

Part II
Fault Properties During
Dynamic Rupture

6

The Transition From Frictional Sliding to Shear Melting in Laboratory Stick-Slip Experiments

David A. Lockner¹, Brian D. Kilgore¹, Nicholas M. Beeler^{1,2}, and Diane E. Moore¹

ABSTRACT

Pseudotachylites are thought to be caused by fault surface melting due to frictional heating during earthquakes. We report on pseudotachylite formation in the laboratory during spontaneous stick-slip on dry, bare-surface granite faults in room temperature triaxial experiments. A continuous melt layer averaging 7 microns in thickness was formed on sawcut surfaces during stick-slip events at 400 MPa confining pressure. At this pressure, dynamic weakening during stick-slip caused total stress drops that ranged from 172 to 414 MPa shear stress (peak normal stress was 249 to 639 MPa) with 1.2 to 4.2 mm slip. In contrast, repeated stick-slip cycles at 50 MPa confining pressure produced fine-grained fault gouge but showed no evidence of melting. Event duration ranged from 0.07 ms for low stress events to 0.32 ms at high stress, and average slip velocity ranged from 0.3 to 20 m/s. Based on thermocouple measurements within 3 mm of the fault, maximum temperatures in some 400 MPa events exceeded 1500°C. By operating at normal stresses 10 to 50 times greater than those used in unconfined rotary machines, triaxial stick-slip experiments are able to develop high transient temperatures and create pseudotachylites, even with limited total slip.

6.1. INTRODUCTION

In recent years, a variety of high-speed rotary shear machines have been developed to measure frictional properties of natural and simulated fault materials at sustained slip speeds as high as ~10 m/s that are representative of coseismic slip speeds [Chang *et al.*, 2012; Di Toro *et al.*, 2004; Di Toro *et al.*, 2011; Han *et al.*, 2011; Han *et al.*, 2007; Hirose and Shimamoto, 2005; Nielsen *et al.*, 2008; Reches and Lockner, 2010; Spray, 2010]. The rapid slip that occurs on a fault during an earthquake can lead to significant frictional heating that under appropriate conditions may cause pressurization of pore water trapped in the fault zone (thermal pressurization) [Andrews, 2002; Noda *et al.*, 2009] and to devolatilization reactions

(dehydration and decarbonation) [Han *et al.*, 2007; Brantut *et al.*, 2008, 2016] that can limit fault heating and lead to dynamic fault weakening [Sulem and Famin, 2009; Brantut *et al.*, 2010; Noda *et al.*, 2009]. Ultimately, continued deformation of narrow principal slip surfaces can lead to melting and the formation of pseudotachylites [Sibson, 1975; Spray, 1987; 2010; Hirose and Shimamoto, 2005; Di Toro *et al.*, 2006, 2009, 2011; Jiang *et al.*, 2015; Proctor and Lockner, 2016]. The work expended per unit area of a fault surface, W , in time interval Δt is

$$W = \tau V \Delta t = \tau \delta = \mu \sigma_n \delta, \quad (6.1)$$

where τ is shear stress, V is slip speed, μ is coefficient of friction, δ is fault slip, and σ_n is effective normal stress. For faults at midcrustal and subduction zone depths, we expect effective normal stress of 50 to 500 MPa or more. Then 1 m slip at, for example, an average shear stress of 100 MPa could raise the temperature of a 4 cm wide shear

¹U.S. Geological Survey, Menlo Park, California, USA

²USGS Cascades Volcano Observatory, Vancouver, Washington, USA

zone by 1000°C. Given the significant energy release that occurs in large earthquakes, it may be surprising that pseudotachylites are not common features of active faults.

In experimental studies, most high-speed rotary laboratory apparatuses are unconfined and are limited to normal stresses of about 20 MPa. The great advantage of these machines is the ability to provide nearly unlimited slip. In this case, low normal stress is offset by extended slip duration so that temperature increases of hundreds of degrees can be achieved through frictional heating. While valuable insights into the evolution of frictional properties of rocks continue to be made with rotary machines, it is important to perform comparable experiments using different fault geometries, sample sizes and, in particular, normal stresses and confinement.

The triaxial test geometry refers to an axisymmetric configuration in which a jacketed cylindrical sample is placed in a chamber that is pressurized with a fluid. Then, deviatoric stress is applied to the sample by advancing a piston against the sample end (Figure 6.1a, b). This test geometry has been used for decades to study rock and fault zone properties at elevated pressures and temperatures appropriate to the mid- to lower-crustal conditions where most of the earthquake hazard resides. Dynamic stick-slip events that occur spontaneously in laboratory tests have been identified as the laboratory equivalent to natural earthquakes [Brace and Byerlee, 1966]. While elevated temperature and pressure are desirable characteristics of the triaxial geometry, a limitation is that fault displacement is generally restricted to less than 15 mm. Furthermore, slip on an inclined fault surface results in dynamic coupling of shear and normal stress. Nevertheless, the ability to conduct dynamic tests on rock at in situ conditions means that high-pressure stick-slip tests in the triaxial geometry can provide observations relevant to earthquake source mechanics. In early experiments [Teufel and Logan, 1978], frictional self-heating and surface melt in the triaxial geometry were proposed. However, questions regarding the stability of the thermal dyes used to infer peak temperature made interpretation of results unclear. Later, Lockner and Okubo [1983] reported heat production during stick-slip on a unique biaxial earthquake simulator, containing a 2 m long fault. Operating at normal stress below 5 MPa, surface temperature increase, based on nearby thermocouple readings, was only a few degrees and heat production accounted for over 90 percent of the energy release. More recently, Koizumi *et al.* [2004], Proctor and Lockner [2016], and Moore *et al.* [2016] have provided convincing observations of surface melt in triaxial granite stick-slip experiments above 150 MPa confining pressure. Passelègue [2014] has reported evidence of flash melting at asperities for experiments run at 50 to 100 MPa confining pressure.

Typical laboratory stick-slip events at low confining pressure report stress drops that are roughly 10% to 20% of peak stress in a biaxial apparatus [Lockner and Okubo, 1983] and a rotary machine [Beeler *et al.*, 2014]. Karner and Marone [2000] reported stress drops on a double direct shear apparatus that ranged from about 10% at high strain rates to about 50% at low strain rates. However, it has been noted that in the triaxial geometry, stress drops can be larger than those produced in the double direct shear geometry and can be correlated with confining pressure. For example, Summers and Byerlee [1977] report 70% stress drops for bare surface and crushed granite layers in granite sawcut experiments at a confining pressure of 630 MPa. In the direct shear and rotary shear geometries, shear and normal stresses are decoupled and dynamic shear stress drops occur at nearly constant normal stress. In the triaxial test configuration, shear and normal stress, as resolved on the fault surface, are coupled. Consequently, dynamic fault slip is accompanied by decreases in both shear and normal stress. The reduction in normal stress should result in a larger stress drop in this configuration, although this effect alone should increase the stress drop by a factor of only about 1.5 [McGarr and Fletcher, 2007]. We will show stress drops ranging from <10% at low confining pressure to 100% above 300 MPa. If we are to relate laboratory stick-slip to natural earthquakes in more than a superficial way, the mechanics that control rupture dynamics in the laboratory must be understood in detail.

In the present study we produce stick-slip events at confining pressures from 40 to 400 MPa (70 to 640 MPa normal stress). Fault surfaces show clear evidence for surface melting at high normal stress. In addition, we find systematic changes in rupture characteristics as a function of normal stress and total work. Thermocouples embedded in the rock within 3 mm of the fault surface record temperature transients that imply average surface heating from about 10°C to over 1500°C. Energy density during stick-slip ranges from 1 to 946 kJ m⁻², and the short slip duration results in an estimated power density as large as 2000 kJ m⁻² s⁻¹. The thin shear zone (<10 μm), short event duration, and large energy density result in the intense surface heating and melt production in these experiments. This combination of conditions will not commonly be found in natural earthquakes, but through proper scaling, the results reported here should provide insight into earthquake processes.

6.2. EXPERIMENTAL PROCEDURE

Room-dry cylindrical samples of Westerly granite with 25.4 mm diameter and 63.5 mm length were tested in a triaxial apparatus at constant confining pressures of 40 to 400 MPa. Samples contained simulated faults that

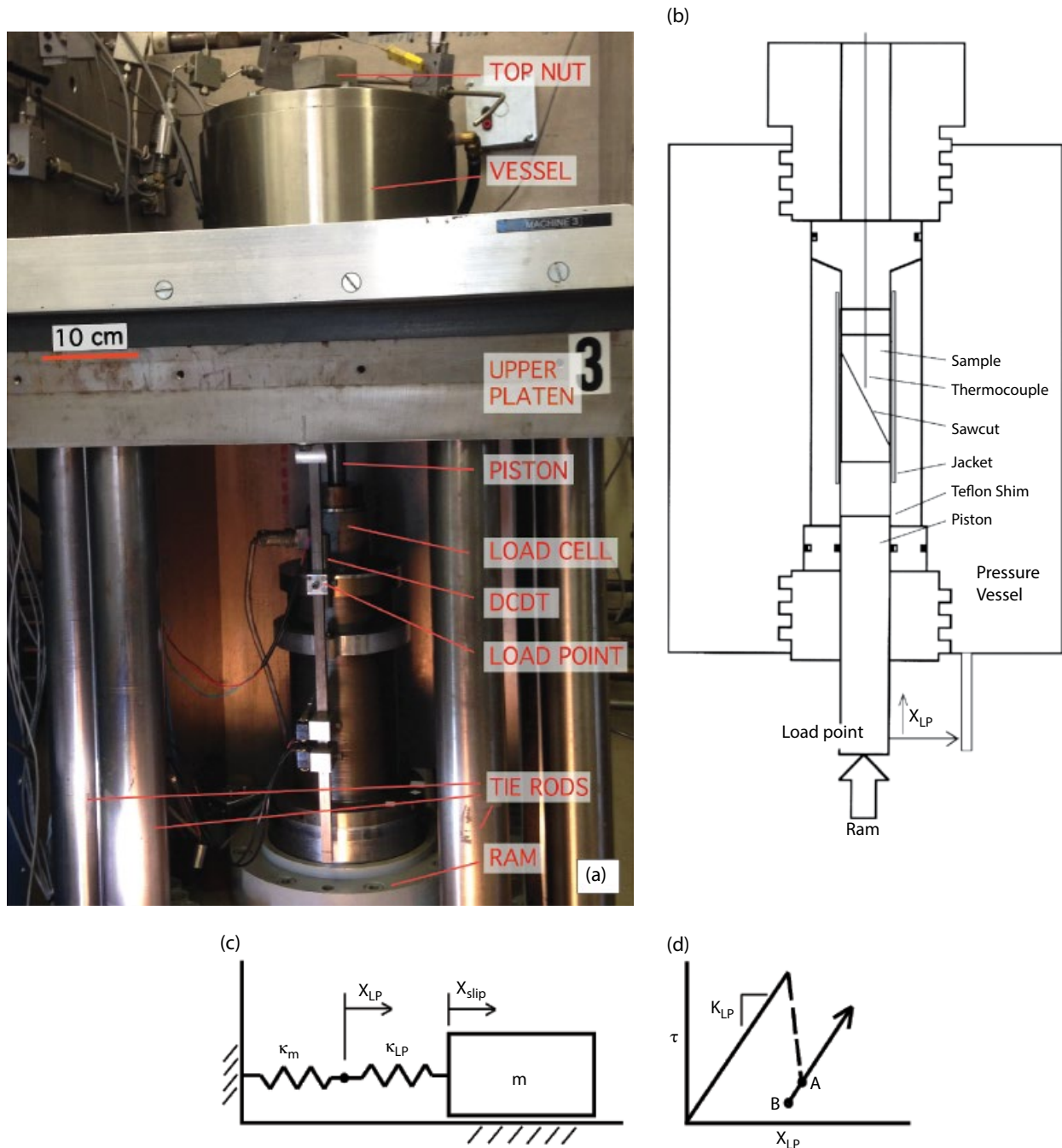


Figure 6.1 (a) Triaxial loading frame used in experiments. Samples are placed in pressure vessel (top) and axial force is applied by hydraulic ram on bottom. (b) Schematic diagram of sample and pressure vessel. Axial load and displacement are measured outside of the pressure vessel. (c) Spring-slider approximation of sample and loading frame. Active servo control eliminates k_m from the system. However, stick-slip events are too fast for servo-control systems to respond and dynamic unloading stiffness is $k_T = 1/(k_{LP}^{-1} + k_m^{-1})$. (d) Representation of stick-slip event with stress plotted versus load point displacement. Solid lines have slope $= k_{LP}$. Stick-slip is represented by dashed line (and has slope $= -k_m$). Following stick-slip, the system comes to rest at point A. Within 3 s, the servo-control system brings load point position back to the control value and reduces stress on the sample to point B. See *electronic version for color representation*.

were sawcuts inclined at an angle $\beta=30^\circ$ to the sample axis (Figure 6.1b). Sawcuts were surface ground and hand lapped with #600 Al_2O_3 abrasive (approximately 15 μm grain size) to provide uniform starting surfaces with 5 to 10 micron roughness. One half of each sample pair had a 1.5 mm diameter hole drilled to within 2 to 3 mm of the simulated fault surface. A 0.6 mm diameter bare K-type thermocouple was embedded at the bottom of each hole with Portland cement to measure heat generated during stick-slip. Thermocouples were small and unsheathed to minimize thermal mass and provide the fastest possible response time. Grout was used, rather than epoxy or other bonding agent, to closely approximate the thermal conductivity and heat capacity of the surrounding granite sample. Additional details of the thermal analysis are presented in section 6.3.8. Samples were placed between steel end caps and slipped into a 3.2 mm wall-thickness polyurethane tube to isolate them from the silicone oil confining fluid.

In each test, the sample was placed in the pressure vessel and confining pressure (P_c) was applied. Then the piston was advanced under computer control using a fast-acting servo-control system. A 0.12 mm greased Teflon shim was placed between the piston and the steel end cap to allow lateral slip of the lower sample half that accommodates shearing on the inclined fault. Axial stress (σ_a) was measured with an external load cell. Axial shortening (x_{LP}) was also measured outside the pressure vessel at the base of the piston using a DCDT displacement sensor. Since the servo system controls the position of this point relative to the pressure vessel, this is referred to as the load point. Slip on the fault surface, δ , is not measured directly. However, it can be computed with reasonable accuracy by accounting for elastic shortening of the sample column according to

$$\delta = \frac{x_{LP} - \frac{\tau}{k_{LP}}}{\cos\beta}, \quad (6.2)$$

where k_{LP} is stiffness of the sample column as determined at the load point (nominally 149 MPa/mm) and τ is shear stress resolved on the sawcut. The test frame is designed to be stiff to minimize the elastic energy stored during loading. Consequently, the stiffness as measured at the load point is dominated by the stiffness of the granite sample and the steel piston. Because these elements are loaded in series, their compliances, defined as the inverse of stiffness, are additive. The granite sample is shorter but has a lower Young's modulus than the piston, so that the elastic shortening of the sample and piston contribute about equally to the load point displacement.

For the inclined fault geometry used in these experiments, shear (τ) and normal (σ_n) stresses resolved on the sawcut are calculated from the measured stresses (axial and confining pressure) according to

$$\tau = \frac{1}{2}\sigma_\Delta \sin 2\beta \quad (6.3a)$$

$$\sigma_n = P_c + \frac{1}{2}\sigma_\Delta (1 - \cos 2\beta), \quad (6.3b)$$

where $\sigma_\Delta = \sigma_a - P_c$ is differential stress. All tests are conducted at constant confining pressure, such that as axial stress increases, both shear and normal stress resolved on the sawcut increase, according to equation (6.3). Finally, as slip occurs on the sawcut, the area of overlap of the two sample halves decreases. This change in area is accounted for in the reported stresses, according to a standard procedure described in *Tembe et al.* [2010, appendix A2]. The true contact area decreases by roughly 3.5% for each millimeter of fault slip.

Data were collected at three different sampling rates. Axial stress, axial displacement, and confining pressure were sampled at 10 samples per second, averaged over 10 consecutive samples and recorded at 1 sample per second. The thermocouple and axial stress outputs were recorded at 100 samples per second (in addition to the 1 Hz axial stress recording). Finally, a laser doppler vibrometer was employed to measure piston velocity during stick-slip to infer slip duration. The vibrometer is a line-of-sight instrument that provides both velocity and distance of a reflective target at 10^6 samples per second. With this device we recorded motion of the piston or load cell near the load point (Figure 6.1). Confining pressure precision is ± 0.1 MPa and accuracy is ± 0.3 MPa. Axial and differential stresses have precision of ± 0.1 MPa and accuracy of ± 0.2 MPa or $\pm 0.2\%$, whichever is greater. Load point position precision is ± 0.2 μm and accuracy is $\pm 0.5\%$.

6.3. RESULTS

6.3.1. General Observations

A total of 112 stick-slip events were recorded in 15 experiments at confining pressures between 40 and 400 MPa as listed in Table 6.1. Normal stress at the onset of stick-slip ranged from 69 to 639 MPa. One hertz data for two representative tests are plotted in Figure 6.2 as shear stress versus fault displacement. The 100 MPa confining pressure experiment contained 17 stick-slip events (diagonal-sloping stress drops) in 8 mm of fault slip. Dynamic stress drops ranged from about 1/3 to 2/3 of peak stress and average slip was about 0.5 mm. By comparison, the fault loaded at 400 MPa confining pressure was significantly stronger and produced two stick-slip events with total stress drops and average slip of about 2.6 mm.

Table 6.1 Stick-slip event parameters.

P_c (MPa)	δ (mm)	τ_p (MPa)	$\Delta\tau$ (MPa)	% $\Delta\tau/\tau_p$	$\sigma_{n,p}$ (MPa)	W_T (kJ/m ²)	T^* (ms)	$\langle V \rangle$ (m/s)	θ_m (°C)	Q (kJ/m ²)	τ_f (MPa)
40	0.0965	54.7	10.9	20	71.6	3.53	0.109	0.9			
40	0.0940	51.0	9.8	19	69.5	3.50					
40	0.0246	50.0	2.2	4	69.0	0.972	0.083	0.3			
50	0.1843	69.1	21.9	32	90.0	9.74					
50	0.1864	70.3	24.2	34	90.6	8.60					
50	0.1823	69.3	22.7	33	90.0	8.91					
50	0.1767	68.1	22.8	33	89.2	7.91					
50	0.1815	72.0	20.9	29	91.7	10.3					
50	0.1892	68.6	24.1	35	89.7	8.58					
50	0.2227	76.3	28.2	37	94.1	11.8					
50	0.3343	76.2	43.3	57	94.2	14.8					
50	0.2108	73.8	24.0	32	92.7	11.9					
50	0.1921	75.5	24.1	32	93.8	10.4					
50	0.1958	75.5	25.2	33	93.8	10.0					
50	0.1757	66.3	20.7	31	88.4	8.91					
50	0.1652	64.3	19.9	31	87.2	8.04					
50	0.1667	64.6	19.7	31	87.5	8.20					
50	0.1651	67.4	21.5	32	89.1	7.35					
50	0.1593	63.4	18.8	30	86.7	7.64					
50	0.1633	63.7	19.5	31	86.9	7.84					
50	0.1721	68.5	22.0	32	89.5	7.73					
50	0.1725	68.6	22.4	33	89.7	7.69					
50	0.1725	68.3	22.5	33	89.5	7.60					
50	0.1669	68.7	21.4	31	89.9	7.72					
50	0.1685	65.1	19.9	31	87.7	8.38					
60	0.1871	78.5	22.8	29	105.5	9.47	0.107	1.7	114	4.33	23.2
60	0.2234	88.4	25.7	29	111.2	12.9	0.132	1.7	118	5.36	24.0
60	0.3700	84.9	44.1	52	108.8	17.7	0.109	3.4	200	8.51	23.0
100	0.3597	113.2	37.1	33	165.6	31.2	0.076	4.7	273	10.2	28.4
100	0.3600	130.5	40.2	31	175.5	34.5					
100	0.3846	113.5	50.2	44	165.7	28.2					
100	0.3795	116.5	38.2	33	167.3	34.2	0.076	5.0	328	12.5	33.0
100	0.3749	113.7	48.5	43	165.7	27.2					
100	0.3375	109.6	43.8	40	163.3	23.8					
100	0.3352	108.0	36.2	33	162.7	27.0	0.125	2.7	200	8.26	24.6
100	0.7756	127.8	89.1	70	174.0	60.2					
100	0.3528	112.5	42.6	38	165.0	29.1					
100	0.3424	123.1	40.1	33	171.1	33.6					
100	0.3382	116.7	34.3	29	167.7	31.4	0.120	2.8	272	13.8	40.8
100	0.3894	120.7	38.7	32	169.8	36.8	0.075	5.2	351	13.4	34.3
100	0.5588	107.5	69.0	64	162.3	36.6					
100	0.5377	106.5	65.3	61	161.8	34.7					
100	0.5280	107.4	67.5	63	162.3	33.3					
100	0.6574	115.9	77.6	67	167.0	46.6					
100	0.5896	108.2	64.1	59	162.7	40.9	0.173	3.4	321	18.1	30.6
100	0.5731	111.2	75.6	68	164.4	35.4					
100	0.4515	133.7	50.9	38	177.4	46.0					
100	0.3950	125.4	39.6	32	172.5	39.2	0.076	5.2	391	15.1	38.3
100	0.3931	117.7	40.0	34	168.0	35.5	0.131	3.0	277	14.7	37.5
100	0.5210	121.5	58.5	48	170.3	41.4					
100	0.5190	105.4	64.2	61	161.0	33.7					
100	0.5175	109.9	69.0	63	163.6	32.1					
100	0.3018	111.6	34.6	31	164.5	23.1					
100	0.3010	116.0	29.7	26	167.2	28.9	0.069	4.4	401	14.8	49.3

(Continued)

Table 6.1 (Continued)

P_c (MPa)	δ (mm)	τ_p (MPa)	$\Delta\tau$ (MPa)	% $\Delta\tau/\tau_p$	$\sigma_{n,p}$ (MPa)	W_T (kJ/m ²)	T^* (ms)	$\langle V \rangle$ (m/s)	θ_m (°C)	Q (kJ/m ²)	τ_f (MPa)
100	0.2955	110.9	34.4	31	164.1	22.3					
100	0.3080	103.1	33.2	32	159.4	23.5	0.122	2.5	170	8.02	26.0
100	0.3056	112.6	34.7	31	164.9	24.5					
100	0.3039	104.3	33.4	32	160.5	23.3	0.115	2.6	175	7.98	26.2
100	0.2542	121.3	28.0	23	169.8	24.1					
100	0.2112	110.5	30.5	28	163.9	14.9	0.102	2.1	203	8.72	41.3
100	0.1968	100.7	22.1	22	158.3	15.1					
100	0.2932	116.7	35.6	31	167.5	21.3	0.104	2.8	191	8.23	28.1
100	0.2908	111.6	33.9	30	164.5	23.3					
100	0.2827	110.9	34.0	31	164.1	21.3					
100	0.3177	110.0	42.5	39	163.9	21.8					
100	0.3174	108.5	42.5	39	162.8	21.8					
100	0.3174	108.3	42.5	39	162.8	22.0					
100	0.3248	105.6	35.0	33	161.3	25.5	0.099	3.3	196	8.00	24.6
100	0.3182	112.9	35.8	32	165.2	25.0					
100	0.3281	105.5	33.4	32	161.1	26.7	0.120	2.7	206	10.1	30.8
100	0.3297	109.0	35.3	32	163.1	27.4	0.072	4.6	283	10.4	31.6
100	0.3115	111.9	35.2	31	164.8	24.1					
100	0.3091	126.0	35.0	28	172.7	29.4					
100	0.3139	113.6	36.0	32	165.5	25.0					
100	0.3136	106.5	39.6	37	161.8	23.4					
100	0.3130	109.2	42.9	39	163.1	21.4					
150	1.2515	172.1	172.1	100	249.2	90.5			659	25.9	20.7
150	1.3129	174.0	174.0	100	250.5	99.5			691	45.2	34.5
200	1.0321	218.2	125.7	58	326.3	144					
200	0.9755	224.4	118.1	53	329.6	148					
200	0.9697	177.6	129.9	73	302.9	89.5					
200	1.3901	211.5	183.0	87	322.1	143					
200	1.1254	190.4	154.3	81	310.4	102					
200	1.0792	187.0	150.1	80	308.3	93.5					
200	0.9423	208.7	118.0	57	320.8	124					
200	0.5853	175.8	67.0	38	301.7	79.5					
200	0.1156	131.8	13.0	10	275.8	14.1					
200	0.4468	155.6	49.8	32	290.0	56.5					
200	0.8231	211.4	94.7	45	321.7	126					
200	0.5451	161.9	72.0	44	293.3	57.2					
200	0.8630	212.2	87.2	41	322.9	134	0.089	9.7	913	39.5	45.8
200	0.8430	210.2	85.3	41	321.7	133	0.089	9.5	748	32.2	38.2
300	2.2736	275.8	235.2	85	459.6	336	0.240	9.5			
300	2.3236	282.6	282.6	100	462.9	312	0.261	8.9			
300	2.4228	275.1	275.1	100	459.0	337	0.299	8.1			
300	3.0698	340.6	340.6	100	496.9	504	0.311	9.9	1332	108	35.1
300	2.9281	313.4	313.4	100	481.1	476	0.303	9.7	1511	118	40.3
300	2.6258	312.5	312.5	100	481.3	390	0.283	9.3	1221	97.4	37.1
300	0.9412	257.2	99.8	39	448.4	164	0.162	5.8	556	36.2	38.4
300	2.0611	272.5	220.9	81	457.7	314	0.131	15.7	1619	85.0	41.2
400	2.9281	340.5	340.5	100	596.1	499	0.221	13.2	1719	118	40.2
400	1.1001	292.2	113.7	39	569.4	229	0.122	9.0	766	41.2	37.5
400	3.0225	327.1	327.1	100	588.9	529	0.157	19.3	2134	121	39.9
400	3.6836	414.4	414.4	100	639.1	758	0.209	17.6			
400	4.2150	385.7	385.7	100	623.4	946					
400	2.7959	350.9	350.9	100	603.1	453					
400	2.3424	312.9	312.9	100	580.5	323					
400	2.3306	293.7	293.7	100	569.5	320					
400	1.9458	255.2	255.2	100	547.9	211					
400	1.2120	302.3	124.8	41	575.0	256	0.093	13.0	996	42.0	34.6
400	2.5692	319.8	319.8	100	584.4	386					
400	1.3360	294.8	125.1	42	570.1	290	0.093	14.4	1013	42.3	31.6

Note: Stresses have been corrected for true area of contact that decreases on the sawcut with continued slip. Displacement is the computed fault-parallel displacement after elastic shortening of the sample, as measured at the load point, has been removed.

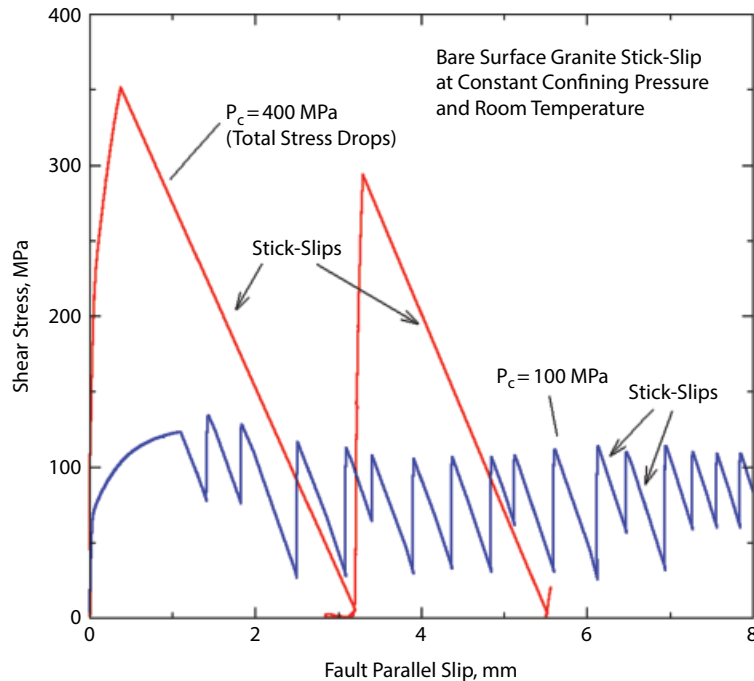


Figure 6.2 Two representative experiments plotting stress versus fault slip at $P_c = 100$ MPa (blue) and 400 MPa (red). Seventeen stick-slip events (diagonal lines) are shown in the 100 MPa test and two events are shown in the 400 MPa test. Not only are displacements much larger at 400 MPa, but the stress drops are complete. See *electronic version for color representation*.

Recorded data for a stick-slip event at 400 MPa confining pressure are shown at three different time scales in Figure 6.3. This was a total stress drop event, with peak shear and normal stresses of 327.1 and 588.9 MPa, respectively, and fault slip of 3.023 mm. Figure 6.3a is a time plot of the 100 Hz data for shear stress, load point displacement, and temperature change as measured 2.4 mm from the sawcut surface. At this time scale the shear stress drop is abrupt. Since the load point displacement is a control parameter, in an ideal experiment it would show a linear increase with time that represents the $2\ \mu\text{m/s}$ imposed loading rate. This appears as the accumulated $100\ \mu\text{m}$ increase in load point position after 50 s. The transient jump in displacement at the time of the stick-slip event is the result of the rapid unloading of the sample column at a rate that is too fast for the servo-control system to respond. The hydraulic servo-valve required 2 s to move the ram back to the computer-prescribed position. The temperature record shows a peak of about 6°C two seconds after the stick-slip event. When compared to the theoretical solution for heat flow from a planar source (section 6.3.8), the computed fault surface temperature exceeded 2000°C . The abrupt 3° transient peak at the time of the stick-slip occurs too soon for a heat pulse to arrive from the fault surface and probably represents local heating of the thermocouple due to distortion of the borehole in response to the violent motion of the stick-slip.

While most of the remainder of the chapter will analyze the low-frequency data, modeling of the frictional heating of the fault surface depends critically on thickness of the sheared gouge layer and slip duration. Prior to each experiment, faults were ground flat and lapped to provide a uniform starting roughness of approximately $10\ \mu\text{m}$. This surface texture was designed so that after only a few tens of microns of slip, a uniform and repeatable layer of fine-grained gouge would be produced. Gouge thickness and melt features are discussed in section 3.7. However, determination of slip duration (rise time, T^*) is problematic when the fault is inside a pressure vessel. As a proxy for a direct measurement of surface displacement, we have recorded velocity of the end of the piston near the load point. Slip of the fault surface will produce a stress wave that travels down the piston. While the overall motion of the piston outside of the pressure vessel will be complex due to multiple reflections in the sample column, we postulate that the initial pulse traveling down the piston provides the duration of the stick-slip event. We therefore measured the velocity of the piston near the load point using a laser vibrometer with a 1 MHz sampling rate. A 100 ms recording of velocity and displacement is plotted in Figure 6.3b. The first 10 ms show a rapid oscillation of the piston followed by a longer period oscillation (approximately 20 ms period) that probably represents ringing of the tie rods connecting the ram to the platen. The beginning of the vibrometer record

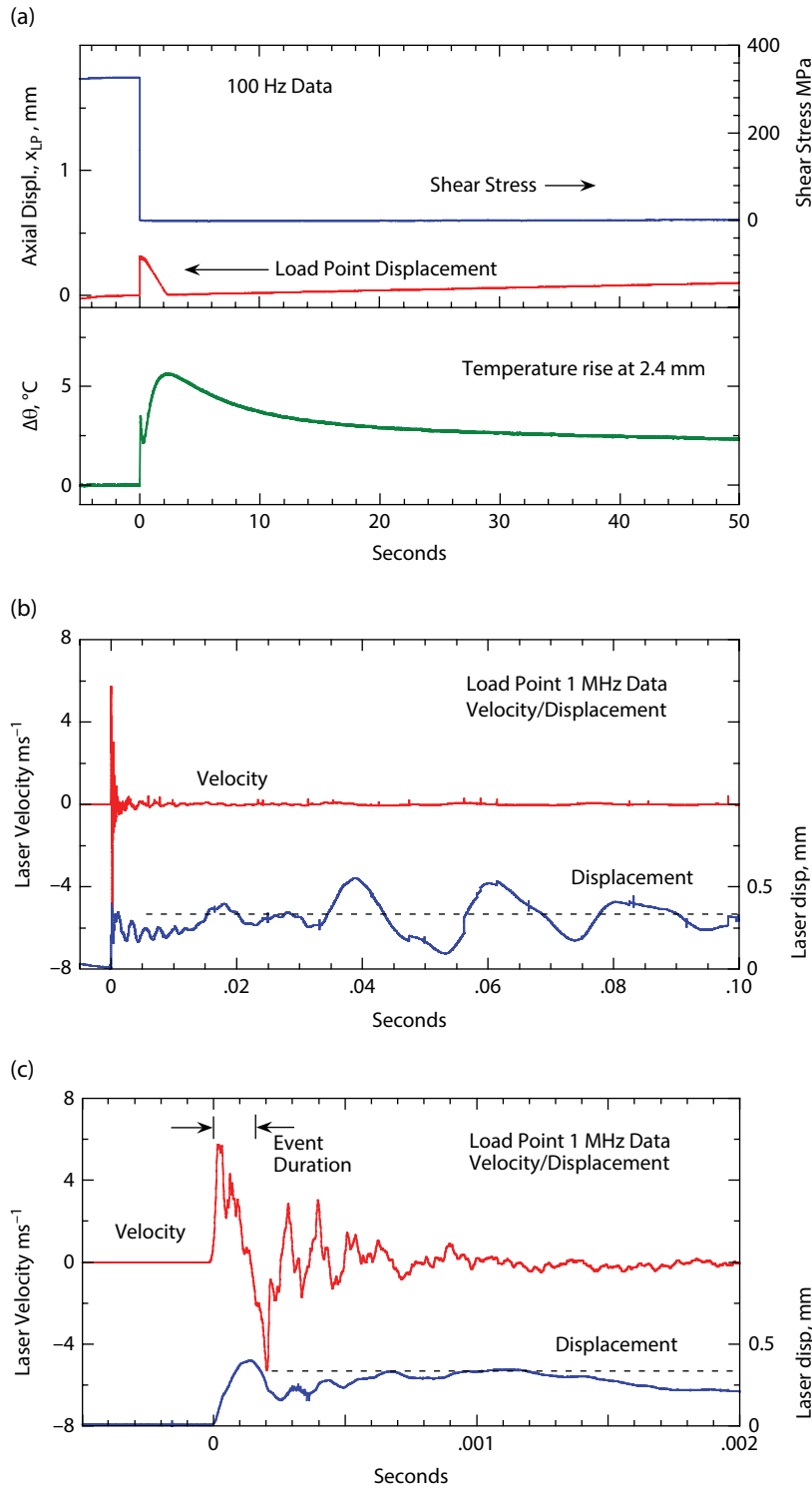


Figure 6.3 A total stress drop stick-slip event is plotted at three different time scales. (a) On a 50 s time scale, the stress drop is abrupt. Displacement jumps ahead about 0.3 mm and requires 2 s for the servo system to regain control. The gradual increase in displacement is the prescribed computer-controlled loading rate. Temperature due to frictional heating is recorded 2.4 mm from the fault surface. A 6°C peak occurs 2 s after the stick-slip and implies a maximum fault temperature $>1500^{\circ}\text{C}$. (b) Velocity and displacement records (from the laser vibrometer recording) for vertical motion of the piston adjacent to the load point (outside of the pressure vessel). In this 100 ms plot, the stick-slip event duration is still not resolved. The 50 Hz vibration probably represents free oscillation of the tie rods excited by the stick-slip event. A constant offset of 0.3 mm occurs at the time of the event. (c) An expanded view showing 2 ms of the high-speed record. Displacement has reached 0.3 mm after 0.16 ms, which we interpret as the event duration. See *electronic version for color representation*.

is expanded to show the first 2 ms of the record following the stick-slip in Figure 6.3c. The dashed horizontal line represents the DC offset in the displacement record following the ring down of the free oscillations of the piston. Notice that the displacement first reaches this level between 0.1 and 0.2 ms. We use this interval as an indication of the stick-slip event duration T^* .

6.3.2. Elastic Unloading Response of Load Frame

Stick-slip instabilities are the result of an interaction of the fault surface, as it undergoes an abrupt loss of shear strength, with the loading frame that provides stored elastic energy [Johnson and Scholz, 1976; Shimamoto *et al.*, 1980; Kilgore *et al.*, 2017 (this volume)]. We begin by discussing some of the characteristics of the loading frame. The deformation machine is designed to be stiff so that it minimizes the storage of elastic energy and thereby reduces the likelihood of stick-slip instability. The general response of triaxial machines has been analyzed in detail, for example, in Shimamoto *et al.* [1980]. Since load-bearing members are made of hardened steel, the machine response to axial load is essentially elastic. In these experiments, stiffness is estimated from

$$k_{LP} = \Delta\tau / \Delta x_{LP}. \quad (6.4)$$

This quantity is specific to our test geometry and sample dimensions, relating shear stress to load point displacement. A more common definition of stiffness relates force, F , to displacement: $\Delta F = \kappa \Delta x$. Because the different components of the load frame are loaded in series (all support the same axial force), it is more convenient to work with compliance, $c = 1/\kappa$, because the compliances of the different elements are additive.

The load point is a convenient position to analyze the quasi-static response of the test machine. For a sample in quasi-static equilibrium, two forces are balanced at the load point: force exerted by the piston and force exerted by the ram (Figure 6.1). The load point position, x_{LP} , refers to the vertical position of the load point relative to the base of the pressure vessel and is one of the parameters measured in the experiment. The direct coupling of elements that exerts force at the load point is piston – sample – top nut – vessel. All elements can be considered elastic and the pressure vessel, given its physical dimensions, is orders of magnitude stiffer than the sample column. The most compliant element is generally the rock sample itself, followed by the steel piston between the sample and the ram. A change in load point position will result in a change in force exerted by the piston as $\Delta F_{piston} = \Delta x_{LP} / c_{LP}$, where c_{LP} is compliance of the sample column. The second force path providing counterforce

between the load point and the pressure vessel is through the machine frame: ram – bottom platen – tie rods – top platen – pressure vessel. These components are all stiff relative to the sample column. When the hydraulic servo-control valve operates, it essentially removes these elements from the system response and c_{LP} becomes the total machine compliance. Since the response time for the servo-valve is 20–50 msec, shorter duration events are too fast for a servo-controlled response and the natural load frame compliance dominates. In this case, compliances of the machine frame components can be lumped together into a single “machine” compliance c_m , and the change in counter force at the load point becomes $\Delta F_{ram} = -x_{LP} / c_m$.

Consider the case immediately before and after a stick-slip event, when the servo-control system has not yet responded. Before the stick-slip, the load point is at a position x_{LP0} and the sample and load frame are supporting axial force F_0 . After stick-slip, the sample column is shortened by the axial component of the slip event $x_{slip} = \delta \cos \beta$, the axial force is reduced by ΔF , and an increment of displacement Δx_{LP} has occurred at the load point. It is simple to show that the load point advances by

$$\Delta x_{LP} = -c_m \Delta F. \quad (6.5)$$

Thus, the rapid jump in load point position accompanying the stick-slip event as shown at time zero in Figure 6.3a provides a direct measure of the machine compliance c_m . Additionally, compliance of the loading column, c_{LP} , can be determined from the slope of the reloading curve following a stick-slip event when the fault surface is locked. Finally, we note that the axial component of fault slip, x_{slip} , can be related to the accompanying decrease in force by

$$x_{slip} = -c_T \Delta F, \quad (6.6)$$

where $c_T = c_m + c_{LP}$. The quantity x_{slip} can be used to compute the change in elastic energy consumed in the stick-slip event. Compliances and stiffnesses for the different system components have been determined as part of the experimental procedure, and values are listed in Table 6.2.

The mechanical response of the loading frame, as discussed in this section, is often represented by a single degree of freedom, lumped-mass, spring-slider model, where the servo-controlled response has a single spring element, k_{LP} , between the load point and the sample, as depicted in Figure 6.1c. The second spring element to the left of the load point, k_m , is eliminated from the system response as long as displacement is controlled by the servo system. However, for slip times shorter than the servo response time, displacement at the load point is no

Table 6.2 Loading frame elastic parameters.

Symbol	Parameter	Value
κ_{LP}	Load point stiffness	149 ± 2 MPa/mm
κ_m	Machine stiffness	1270 ± 60 MPa/mm
κ_T	Total stiffness	133 ± 3 MPa/mm
κ_{LP}	Load point force stiffness	174 ± 2 kN/mm
κ_m	Machine force stiffness	1480 ± 70 kN/mm
κ_T	Total force stiffness	156 ± 5 kN/mm
c_{LP}	Load point compliance	$(5.75 \pm 0.11) \times 10^{-9}$ m/N
c_m	Machine compliance	$(0.675 \pm 0.034) \times 10^{-9}$ m/N
c_T	Total compliance	$(6.43 \pm 0.19) \times 10^{-9}$ m/N

longer actively controlled and the response is more like the full double spring system depicted in Figure 6.1c. This simple model has been successful in representing laboratory stick-slip [Johnson and Scholz, 1976; Rice and Tse, 1986; Kilgore *et al.*, 2017 (this volume)]. For very rapid stick-slip, the lumped mass model may no longer be appropriate as distribution of mass in the sample, piston, and other elements becomes important and a fully dynamic solution is required. This situation is discussed further in the following sections.

6.3.3. Calculating Stress Drop and Total Slip

High-speed displacement, velocity, and stress data were recorded for only a limited number of stick-slip events. Consequently, we developed a method for determining stress drop and displacement from the slow 1 Hz data. Since the applied loading rate was slow, the stress and displacement at the onset of each stick-slip event are well determined in the 1 Hz data. Following each stick-slip, the fault surfaces come to rest and lock up with no indication of measurable afterslip. Thus, the reloading curve following stick-slip constrains the ending stress and displacement. The problem becomes determining ending stress and displacement as depicted by point A in Figure 6.1d from stress and displacement recorded one to two seconds later in the 1 Hz data. The rapid displacement reversal following the stick-slip event in Figure 6.3a represents the servo-control valve moving the ram backward at full speed and bringing the load point position back to the computer-prescribed position. The displacement rate of the ram and accompanying unloading rate of the sample column are determined from plots like Figure 6.3a. In addition, the displacement adjustment in the seconds following stick-slip is proportional to the stress change between points A and B in Figure 6.1d, according to equation (6.4). This is all that is needed to calculate the ending stress and displacement of the fault surface from the apparent stress and displacement as recorded at 1 Hz.

6.3.4. Observed Stress Drop and Slip

Data for the 112 recorded stick-slip events are listed in Table 6.1. Confining pressure ranged from 40 to 400 MPa and resulted in peak shear stress, τ_p , spanning 50 to 414 MPa. Associated shear stress drops, $\Delta\tau$, ranged from 2.2 to 414 MPa. In all, 16 of the highest normal stress stick-slips underwent total stress drops. Peak stress is plotted as a function of peak normal stress for the full catalog of 112 events in Figure 6.4a. Following equations (6.3a) and (6.3b), experiments run at the same confining pressure form a locus of points on a line with slope = $\sin 2\beta / (1 - \cos 2\beta) \approx 1.732$. This results in the linear groupings of events in Figure 6.4. Peak stress, even for stick-slip events under nominally identical conditions, shows considerable variability, having a standard deviation of roughly 9% of the average value at each confining pressure. This variability, especially at higher pressure, may reflect differing degrees of welding of the slip surface following melting in previous slip events [Proctor and Lockner, 2016]. The same strength data are replotted as coefficient of friction $\mu = \tau/\sigma_n$ in Figure 6.4b. Coefficient of friction at peak stress is often referred to as the static coefficient of friction. These friction values show a gradual decrease with increasing normal stress, consistent with Byerlee's law [Byerlee, 1978].

In Figure 6.5 we plot shear stress drop $\Delta\tau$ as a function of τ_p . Lines of constant percent stress drop are included for reference. There is an overall trend of increasing stress drop with increasing peak stress with a power law exponent of about 1.6. When events are sorted by peak stress, the lowest quartile has an average stress drop of 22 MPa while the upper quartile has an average stress drop of 229 MPa.

We next look at how stress drop varies with fault slip. In the simple spring-slider model, unloading rate is determined by the machine stiffness $\kappa_T = 1/c_T$ where, as we discussed previously, the lumped compliance $c_T = c_{LP} + c_m$. In this case, stress drop should vary with fault slip according to equation (6.6). We test this prediction in Figure 6.6, which is a log-log plot of change in axial force versus Δx_{slip} . Load point stiffness κ_{LP} (=174 kN/mm) and total stiffness κ_T (=156 kN/mm) are plotted for reference. While data are bounded by κ_T , many data points fall as much as 20% below the stiffness curve, indicating more slip than expected. The total stress drop events are overdriven and come to rest with a gap between the piston and the sample column. If this gap opens while slip is still occurring on the fault, the assumption that the system is unloading elastically at a rate given by κ_T is no longer valid and excess slip can occur. By a similar argument, the loading frame tends to become stiffer with increasing confining pressure. So dynamic unloading may have an initial slope of $-\kappa_T$ that then becomes smaller for the larger stress

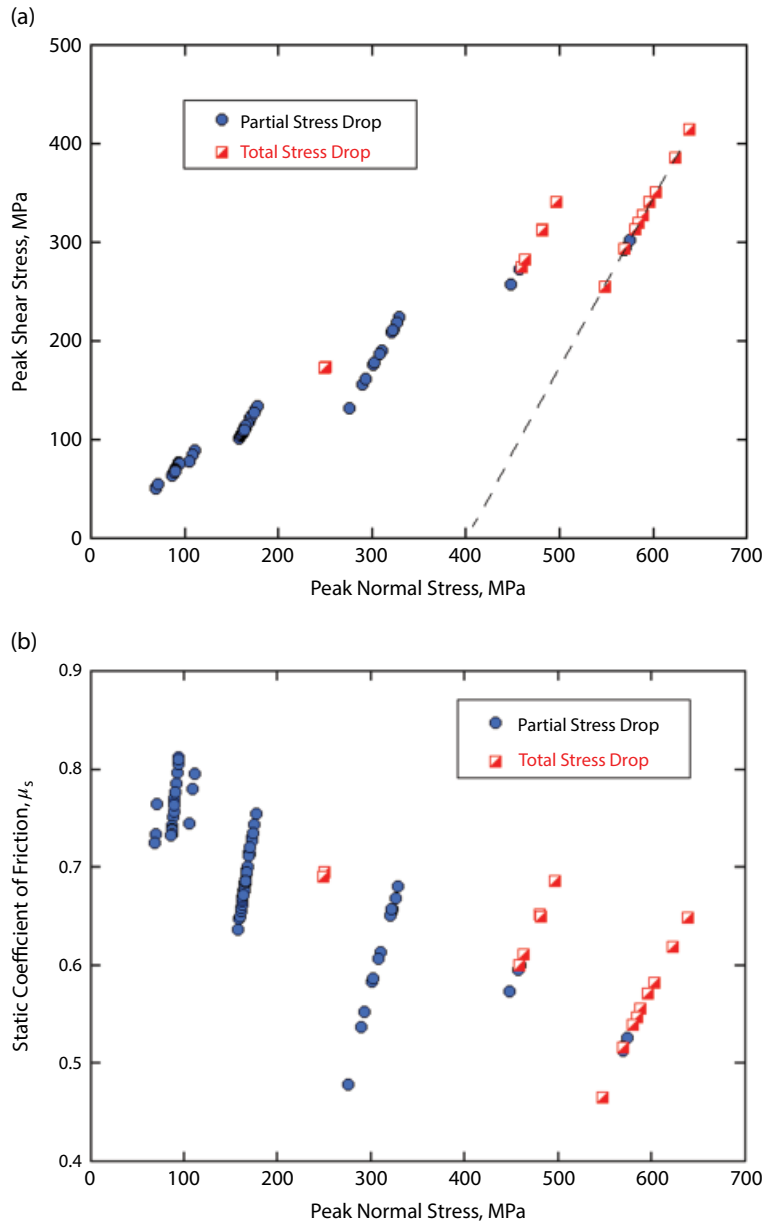


Figure 6.4 (a) Peak shear stress plotted versus peak normal stress at the onset of stick-slip for all 112 events. At constant confining pressure, shear and normal stress increase along a loading path of fixed slope determined by the sawcut angle (equation [6.3]). The events that are farthest to the right, for example, were run at $P_c=400$ MPa. Nearly all of these were total stress drop events. While increased confining pressure tends to result in increased strength, there is notable variability in peak stress for tests run at each confining pressure and therefore under nominally identical conditions. The sequence of 100 MPa events plotted in Figure 6.2 demonstrates this variability. (b) The same events are plotted as peak (static) coefficient of friction. The decreasing trend in friction follows Byerlee's law. See *electronic version for color representation*.

drop events. These details are not well quantified and the variations in apparent stiffness shown in Figure 6.6 may be a measure of uncertainty in our stress drop and total energy calculations. In Figure 6.7, we plot predicted fault-parallel slip, based on stress drop and κ_r , as a

function of observed fault-parallel slip for total stress drop stick-slip events. Although four events came to rest at the expected slip, many events slid more than 0.5 mm beyond the point where the driving force that the piston imparted to the sample had dropped to zero.

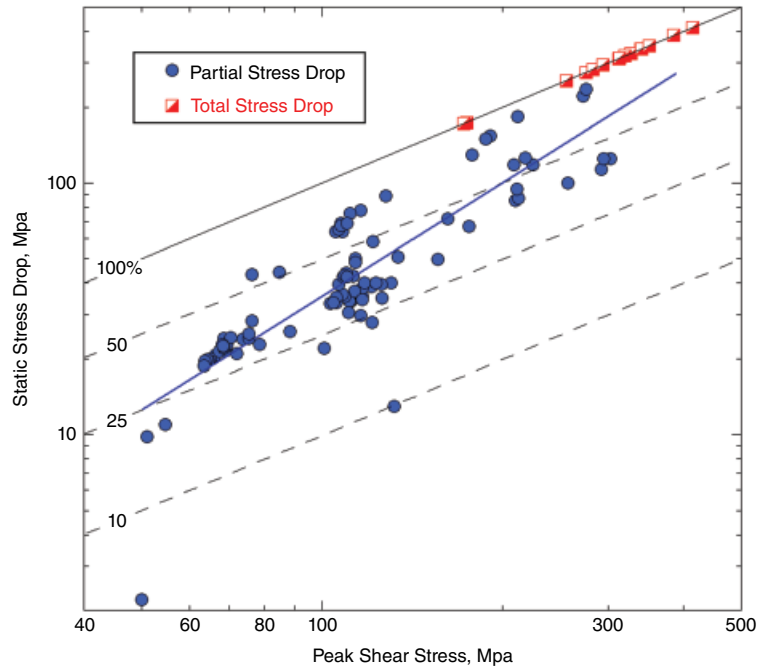


Figure 6.5 Static shear stress drop is plotted versus peak shear stress. Total stress drop events are shown as red squares. Diagonal lines represent constant percent stress drop. There is a gradual increase in percent stress drop with increasing confining pressure. See *electronic version for color representation*.

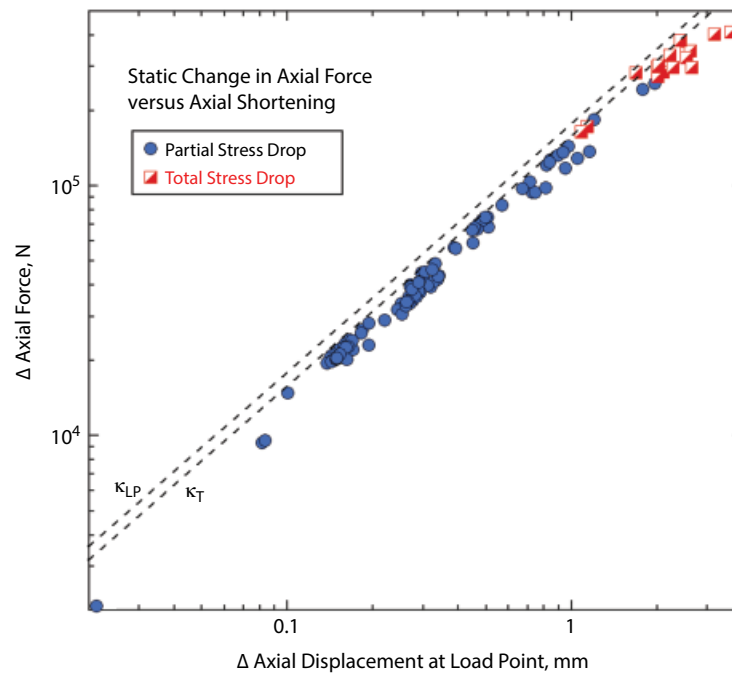


Figure 6.6 Change in axial force plotted versus axial shortening due to slip on the sawcut. Since stick-slip happens faster than the servo-control response, unloading response should fall along the lower dashed line that represents the total system stiffness, κ_T . See *electronic version for color representation*.

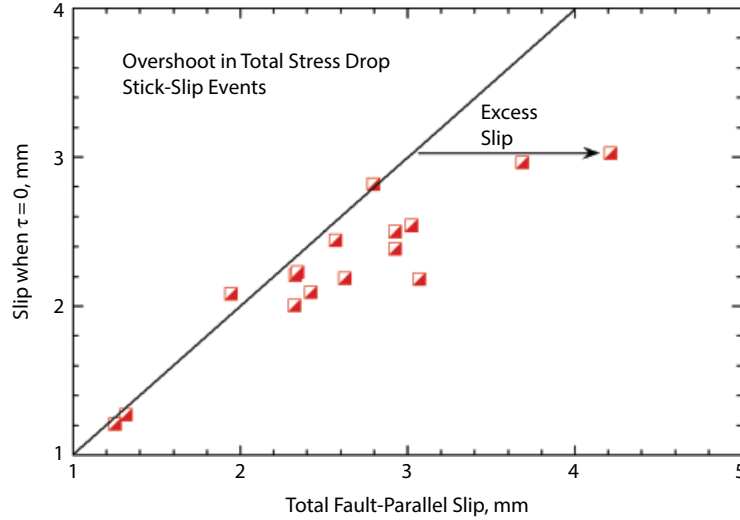


Figure 6.7 Horizontal axis represents measured fault slip for total stress drop events. The vertical axis is computed fault slip when shear stress has dropped to zero ($\Delta\tau = -k_r \Delta\delta$). Events that plot to the right of the diagonal line have continued to slide (presumably driven by stored kinetic energy) past the point where they are driven by the piston. See electronic version for color representation.

6.3.5. Total Energy Release

Stick-slip event durations are so short that the servo-control systems cannot respond until slip has ended. In this case, the sample and loading frame can be considered a closed system in which stored elastic energy is consumed without input of energy from the surroundings (i.e., no additional work done by hydraulic pumps or other control systems). If the frame unloads linearly with slip on the fault, the change in elastic energy of the load frame is

$$\Delta E_{el} = \frac{1}{2}(F_p + F_e)\Delta x_{slip}, \quad (6.7)$$

where F_p and F_e are axial force at the start and end of the stick-slip event.

There is a net displacement of the piston into the pressure vessel during the stick-slip events, resulting in $\int PdV$ work as the confining fluid is compressed. Work in compressing the confining fluid varies with confining pressure and on average represents 37% of the total energy release. This work is part of the response of the loading system and not related to fault properties. Consequently, we subtract it from the elastic energy release (equation [6.7]) and report the resulting energy, normalized by the fault surface area, as total work W_T . This total work is plotted as a function of fault parallel slip in Figure 6.8. As expected, W_T increases with increasing slip. A power law fit to the partial stress drop events gives

$$W_T [\text{kJ m}^{-2}] = 121\delta^{1.44}, \quad (6.8)$$

with δ measured in mm. The total stress drop events, on average, have 25% greater slip than would be predicted by the partial stress drop events.

6.3.6. Slip Duration and Velocity

Stick-slip event duration becomes important in modeling the temperature rise that occurs due to frictional heating of the fault surface. Event duration is difficult to measure directly on a fault surface inside the pressure vessel at high pressure. An internal load cell was constructed to obtain a near-field measure of stress drop, but unfortunately it malfunctioned. As explained in section 6.2, slip duration is inferred from motion of the piston outside the pressure vessel near the load point. Vertical velocity and displacement of the top surface of the load cell, adjacent to the load point, were sampled at 1 MHz in 37 experiments using a laser doppler vibrometer. The estimates of slip duration range from 0.07 to 0.32 ms and are plotted as a function of total slip in Figure 6.9. Lower energy/shorter slip events tend to cluster with event durations averaging $T^* = 0.11$ ms and average slip $\delta = 0.59$ mm. Average velocity of these events is therefore 5.4 m/s. Total stress drop events have longer durations averaging 0.27 ms and larger slip (average slip = 2.76 mm). Average velocity for total stress drop events is 10.2 m/s, about twice as fast as the smaller events. The largest average velocity of 19.3 m/s was recorded for a total stress drop event at 400 MPa confining pressure.

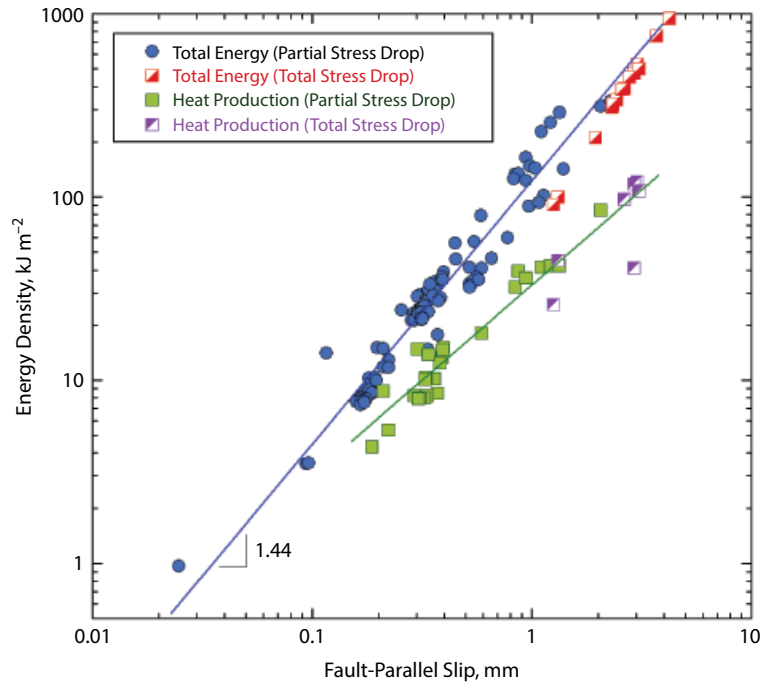


Figure 6.8 Blue and red symbols are total energy release in stick-slip events calculated from total slip and average unloading stress. Green and purple squares are heat generated during stick-slip as inferred from 1D heat flow model and the temperature rise recorded by thermocouples 2 to 3 mm from the fault surface (see section 3.8). The proportion of energy that results in heating of the fault is less for high confining pressure events that produce surface melt. See *electronic version for color representation*.

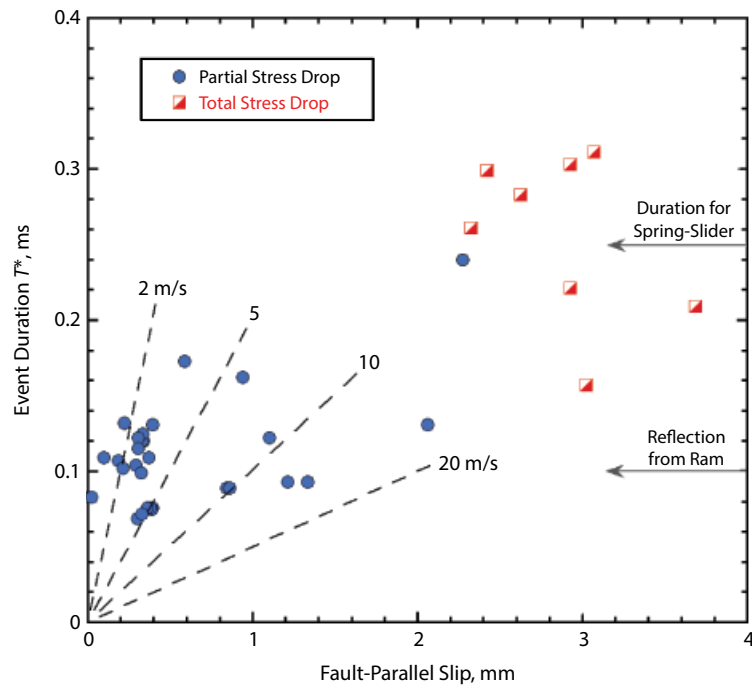


Figure 6.9 Event duration plotted versus fault slip. Events tend to cluster into two groups. High-stress events that produce surface melt have more than twice the slip duration and five times the total slip of the low-stress stick-slips. Average slip speeds vary from about 1 m/s for the low stress events to as much as 20 m/s for some total stress drop events. Indicated on right is event duration predicted by lumped-mass spring-block model ($T^* = 0.25$ ms). Also shown at 0.1 ms is predicted arrival at the fault of the wave traveling down the piston and reflected back from the load cell (see Figure 6.1A). See *electronic version for color representation*.

6.3.7. Characterization of the Fault and Surface Melting

Scanning electron microscope (SEM) images were made of selected samples by either separating the sample halves along the sawcut or by epoxying samples together and cutting parallel to the cylinder axis and perpendicular to the sawcut. Prior to each experiment, samples were prepared by surface grinding the sawcuts and then hand lapping with #600 Al_2O_3 abrasive to provide a uniform starting roughness of approximately $10\mu\text{m}$. Secondary-electron (SE) SEM images (Figure 6.10) show the texture of the starting surfaces. Individual grains have been plucked from the sawcuts during grinding. Otherwise, surfaces are flat at long wavelengths with a scalloped

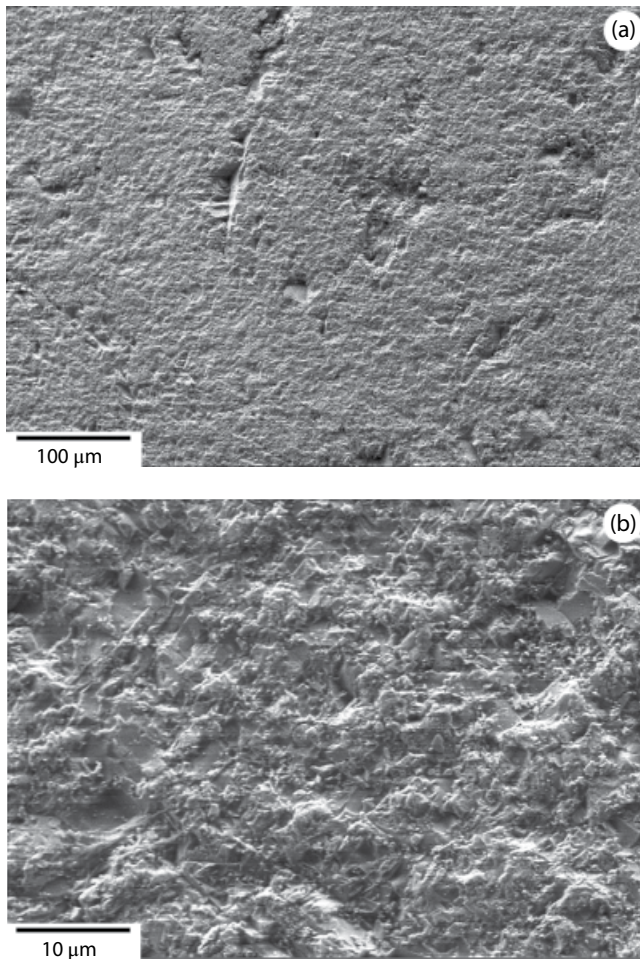


Figure 6.10 Secondary-electron (SE) SEM images of initial roughness of granite surfaces after hand lapping with #600 Al_2O_3 grit. All samples were prepared in the same manner. (a) Low-magnification view, showing scattered deep pits produced by plucked grains. (b) Close-up image of a feldspar, whose surface topography is influenced by its two nearly perpendicular cleavages.

texture over distances $<20\mu\text{m}$. This initial fault roughness was chosen so that after only a few tens of microns of slip, a uniform layer of fine-grained gouge would be produced.

An example of the sliding surface after 8.8 mm slip and 22 stick-slip events at 50 MPa confining pressure is shown in Figure 6.11. These SE SEM images show that a fine-grained gouge has developed on the sawcut and slip was localized along slickensided Y or boundary shears. Polished thin-section, backscattered-electron (BSE) SEM images of a sample after 8.6 mm slip and 19 stick-slip events at 100 MPa confining pressure are shown in Figure 6.12. Sawcut surfaces separated slightly during removal from the pressure vessel and prior to injection of epoxy. Average gouge layer thickness in the thin section images was $7\mu\text{m}$ with a range of $2\text{--}16\mu\text{m}$. This gouge layer thickness becomes important in estimating the temperature rise due to frictional heating in the stick-slip events. Figure 6.12b shows a dark band (between the white arrows) that could represent a slip surface equivalent to the slickensided shear in Figure 6.11. If this is the actual principal slip surface (PSS) and the rest of the gouge layer does not shear during stick-slip, sliding is occurring on a remarkably thin layer ($<0.5\mu\text{m}$). We will use a range of PSS thickness between zero and $7\mu\text{m}$ in our thermal calculations to include the possible range of surface heating during stick-slip.

No evidence for surface melting was found in either the 50 or 100 MPa confining pressure SEM images. Instead, surfaces were separated by a thin layer of granular gouge formed by grinding and crushing of the approximately $10\mu\text{m}$ surface roughness (Figure 6.10) of the preroughened faults. Some grain fragments were as much as $10\mu\text{m}$ in size, reflecting the starting surface roughness. However, the majority of grains are submicron in size. In some cross-sectional images, coarser grains fill depressions in the sawcut surfaces that apparently represent voids left by grains plucked during surface grinding. These large sheltered grains appear in stark contrast to the fine grains that constitute the PSS due to comminution during shearing.

Fault surfaces of samples deformed at 400 MPa confining pressure have a remarkably different appearance from samples deformed at low pressure. When sample halves are separated, surfaces are usually bonded (welded) on the sawcut and separate irregularly within the weakened damage zone adjacent to the sawcut. SEM images from two samples are shown in Figure 6.13. Secondary-electron photos (Figure 6.13c, d) are taken from a sample that underwent 4.1 mm of combined slip in a partial stress-drop stick-slip followed by a total stress-drop stick-slip. These images are compared to backscattered-electron images (Figure 6.13a, b, e, f) of a second 400 MPa test sample that underwent a similar partial and then total

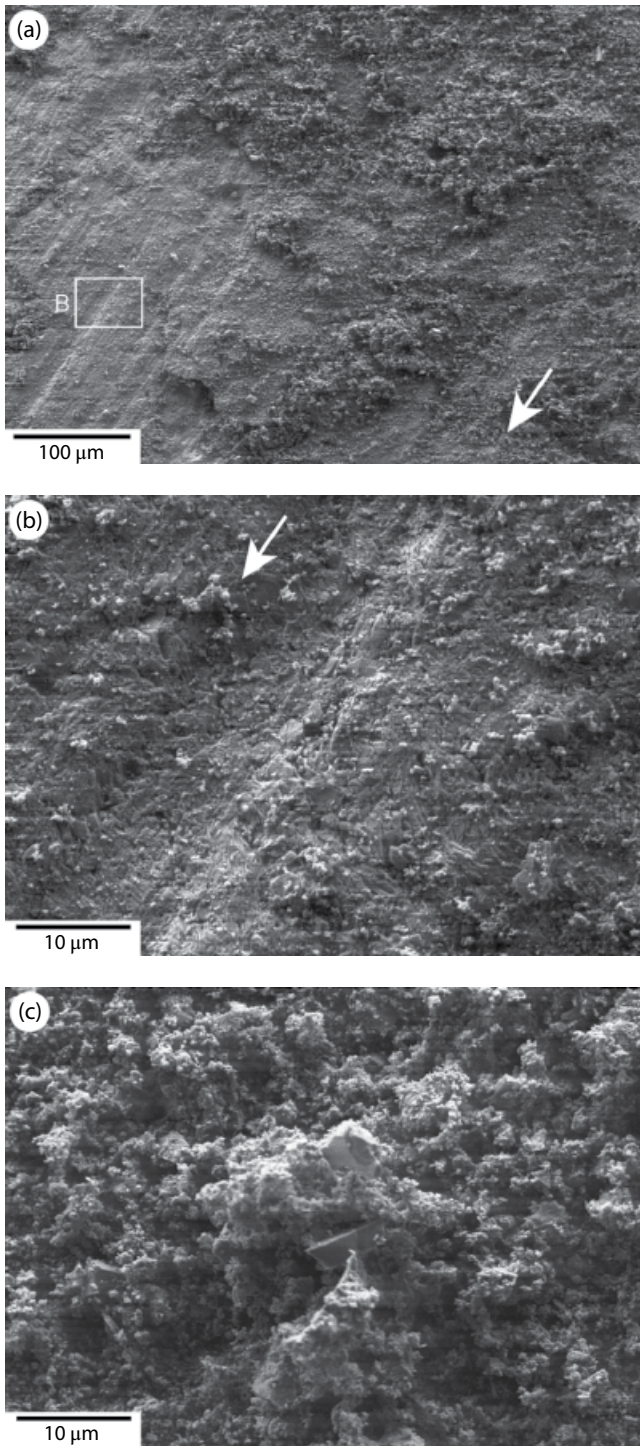


Figure 6.11 SE images of one of the sawcuts after shearing at 50 MPa confining pressure. White arrows show the direction of motion of the granite block. (a) Slip is localized along slickensided subsidiary shears in a layer of fine-grained gouge developed between the sawcuts. The white box shows the location of (b). (b) and (c) are higher-magnification views of the rough-textured slickensided surface and the loose, granular gouge overlying it, respectively.

stress-drop stick-slip sequence with combined slip of 4.4 mm. As seen in cross-section (Figure 6.13a, b), groups of elongate voids span the lengths of phyllosilicate minerals adjoining the sawcuts. The delicate filaments that crisscross the openings (Figure 6.13b) may correspond to the glassy structures visible on the sawcut surfaces (Figure 6.13c, d). To be so well preserved, these structures must have formed at the end of the final, total stress drop stick-slip. The shears are considerably less porous where situated between quartz and feldspar minerals (Figure 6.13e, f); no large voids were seen, although some stretched vesicles are present (Figure 6.13f). In addition, fragmented crystals in the damage zone adjacent to the shears, for example, the clast-filled depression in Figure 6.13f, appear to be fused together by vesicular glass. Compositional layering across the thickness of the shears is common. The bright central band of the shear in Figure 6.13e (total thickness indicated by the black bar) and the bright streaks of the shear in Figure 6.13f are enriched in Fe, Ti, and Mg derived from biotite. Many additional photos of melt textures are presented in *Moore et al.* [2016].

6.3.8. Frictional Heating of the Fault Surface

In this section we analyze temperature transients following stick-slip from thermocouples grouted in axial boreholes at a nominal distance of 2.5 mm from the sawcut surface. A representative thermocouple output, recorded at 100 Hz, is plotted in Figure 6.3a. A temperature transient with peak value of 6°C occurred approximately 2 s after the stick-slip event. As described in the following analysis, this represents heating of the fault surface of more than 1500°C. Usable temperature recordings were obtained from 34 stick-slip events. A convenient scaling quantity for 1D heat flow is the thermal half width $a_0 = (4\alpha t)^{1/2}$, where α is thermal diffusivity. The thermal half width represents the approximate distance that a thermal pulse will propagate in time t . Consistent with *Lachenbruch* [1980], we use granite diffusivity of $\alpha = 1.2 \times 10^{-6} \text{ m}^2 \text{ s}^{-1}$ throughout our calculations. Then, for an inclined fault surface with semiminor radius of 12.7 mm, a 1D approximation for heat flow near the center of the fault can be used for nearly 30 s before 3D sample geometry becomes important. A thermocouple 2.5 mm from the fault should see a time delay of 0.5 to 1 s for heat conducting away from the slip surface. We use a 1D heat flow analysis, following *Cardwell et al.* [1978] and *Lachenbruch* [1980], to fit the temperature histories following stick-slip for thermocouple distance and total heat production. Then, using our estimates of slip duration and gouge width, we back-calculate the maximum temperature on the fault. A similar procedure was used by *Lockner and Okubo* [1983] to model heat production on a large biaxial press.

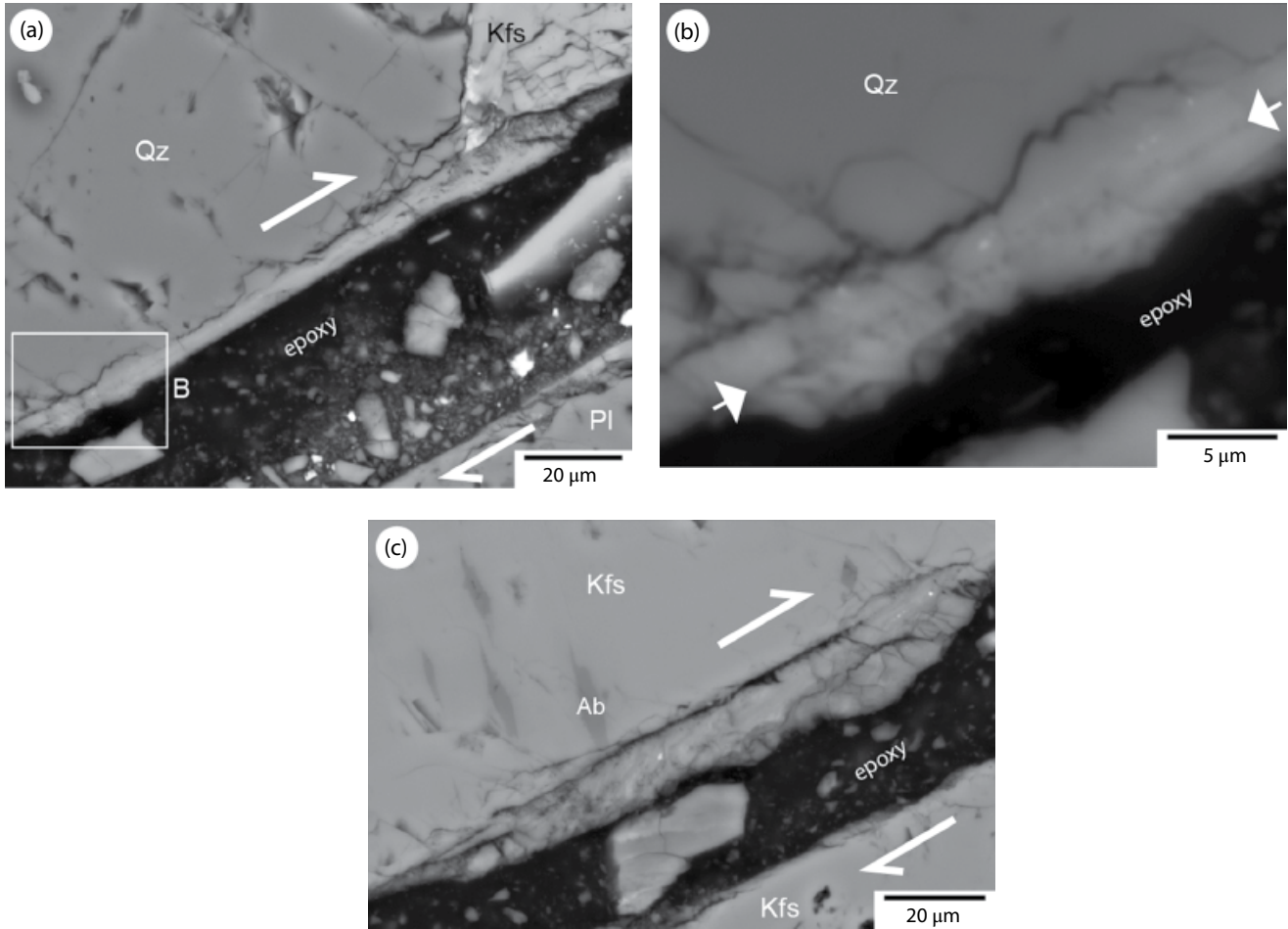


Figure 6.12 Deformation textures developed along the sawcut after slick-slip at 100 MPa confining pressure. The sample was sectioned perpendicular to the sawcut and parallel to the cylinder axis; backscattered electron (BSE) SEM photos are oriented to show right-lateral shear (indicated by paired white half-arrows). (a) Lower- and (b) higher-magnification views of the gouge layer, which is finer grained, on average, than that formed at 50 MPa. The faint dark line down the center of the gouge layer (between the white arrows in B), may be a slip surface equivalent to the slickensided shear in Figure 6.11. The gouge appears to consist of “clasts” of denser (brighter) gouge in a more porous matrix. (c) Fragmentation of earlier-formed, dense gouge in one or more subsequent stick-slip events. Abbreviations: Ab, albite; Kfs, K-feldspar, Pl, plagioclase, Qz, quartz.

For simplicity, we assume that the PSS has thickness $2a$ and is represented by the gouge zone thickness as observed in the SEM images. We further assume uniform strain rate within the gouge during a stick-slip event. Since there is some indication that the PSS for an individual stick-slip event may actually be ten times narrower than the gouge layer (see preceding section), assigning shearing to the entire gouge layer will provide a lower bound on the estimate of maximum temperature. We see no evidence for injection of the melt into the wall rock. Furthermore, we see no evidence for melting of wall rock or significant widening (by melting) of the PSS, and unlike high speed rotary experiments that are unconfined, gouge is not ejected from the fault zones in our confined tests. Consequently, the measured thickness of the PSS as

presented in images like Figures 6.12 and 6.13 provides an accurate upper bound on the width of the melt layer during stick-slip. For times following the stick-slip duration (denoted by T^*), temperature rise at distance x from the fault axis is given by [Cardwell *et al.*, 1978]

$$\theta(x,t) = \theta_0 + \frac{Q}{4\rho c_p a T^*} \int_0^{T^*} \left\{ \operatorname{erf} \left[\frac{x+a}{(4\alpha [t-t_0])^{1/2}} \right] - \operatorname{erf} \left[\frac{x-a}{(4\alpha [t-t_0])^{1/2}} \right] \right\} dt_0 \quad t > T^*, \quad (6.9)$$

where the integral is evaluated numerically. Here, θ is temperature, ρ is density, c_p is specific heat, a is shear zone

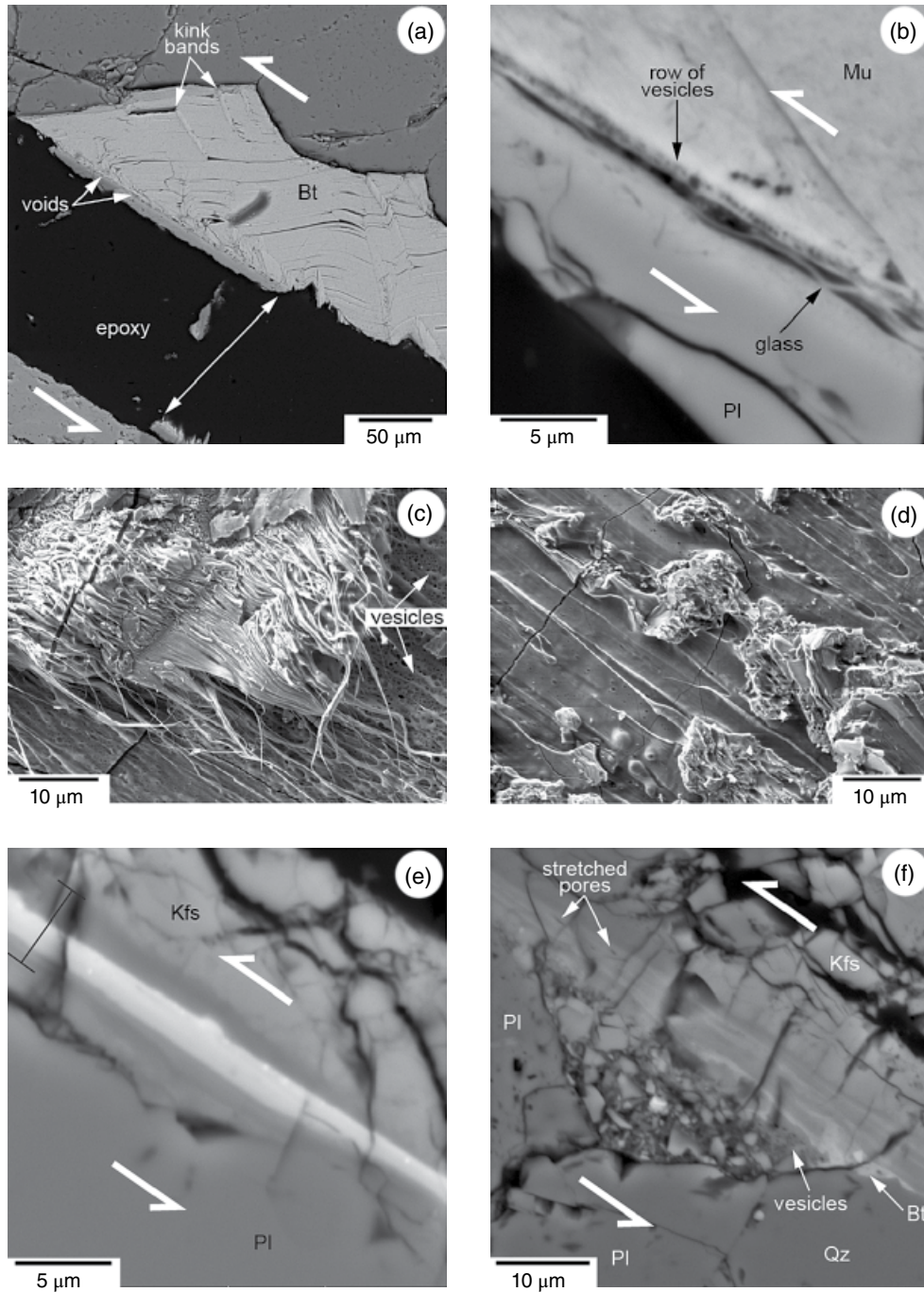


Figure 6.13 Glass textures in SEM images from two samples deformed at 400 MPa confining pressure. (a) and (b) Textures developed adjacent to phyllosilicate minerals (BSE images). The driving blocks were welded together at the shear and typically separated along adjoining, weakened damage zones. The PSS at the base of the kinked and folded biotite (Bt) in (a) is marked by a row of elongate voids. In B, glassy filaments crisscross an elongate void between muscovite (Mu) and plagioclase (Pl). A row of vesicles (≤ 500 nm diameter) marks the base of the muscovite. (c) and (d) Glassy textures in views looking down on the sawcut (SE images), including glassy filaments, glassy surface coatings, and rounded and stretched vesicles that indicate degassing. (e) and (f) Shears located between feldspar (Pl, Kfs) and quartz (Qz) crystals are devoid of large voids and commonly are compositionally layered (BSE images). The bright central zone in (e) is enriched in elements obtained from biotite (K, Fe, Ti, Mg); total shear thickness is indicated by the black bar. The shear in (f) contains a few stretched pores, and the matrix of the debris-filled pit sealed off by the shear appears to be vesicle-filled glass.

half width, and Q is total heat generated per unit cross-sectional area of the fault during stick-slip. If τ_{av} is average shear stress on the fault during stick-slip, then $Q \approx \tau_{av} \delta$. Q includes the heat of melting PSS material rather than increasing temperature and would not be accounted for in the thermal modeling. This turns out to be a relatively small correction and is discussed below. In our calculations we use $\rho = 2800 \text{ kg m}^{-3}$ and $c_p = 840 \text{ J kg}^{-1} \text{ }^\circ\text{C}^{-1}$. Equation (6.9) assumes uniform heat production within a zone of thickness $2a$ and at constant rate over the time interval $[0, T^*]$. If melt is produced during stick-slip, dynamic shear resistance may vary significantly both with time and position on the fault surface. Still, given the limited data available, this 1D model is appropriate for placing basic constraints on fault heating and energy release. *Cardwell et al.* [1978] note that the maximum possible temperature rise occurs when $a < a_\theta$ and is given by

$$\theta_m - \theta_0 = \frac{Q}{\rho c_p (\pi \alpha T^*)^{1/2}}. \quad (6.10)$$

During and after stick-slip, the maximum temperature will be at the center of the PSS. Therefore, in the model, maximum temperature following stick-slip is given by

$$\theta_{x=0} = \theta_0 + \frac{Q}{2\rho c_p a T^*} \int_0^{T^*} \left\{ \text{erf} \left[\frac{a}{(4\alpha [t-t_0])^{1/2}} \right] \right\} dt, \quad t > T^*. \quad (6.11)$$

Estimates of slip duration from the laser vibrometer data range from 0.07 to 0.32 ms (see above). Thus, the thermal half width at the end of stick-slip events is estimated to be between 18 and 39 μm . Average gouge half-width from the SEM images described in the preceding section was 3.5 μm , although the dynamic PSS in individual stick-slip events might be significantly less than this. We conclude that for the fault geometry tested here, $a/a_\theta = 0.09\text{--}0.2$ at time T^* and both event duration and fault width are important in limiting maximum temperature (equation [6.11]). Maximum PSS temperature is estimated by fitting equation (6.9) to the thermocouple recordings between 1 and 4 s (Figure 6.14).

Before presenting results, we consider the accuracy of the thermal modeling. Narrow PSS and short event duration mean that peak temperatures, measured just 2.5 mm from the fault, are less than 0.5% of the modeled peak temperatures on the fault surface. Thermocouples are grouted into a blind hole with an accuracy of about $\pm 0.1 \text{ mm}$. This produces an uncertainty in estimating peak temperature of ± 5 percent. Uncertainty in event

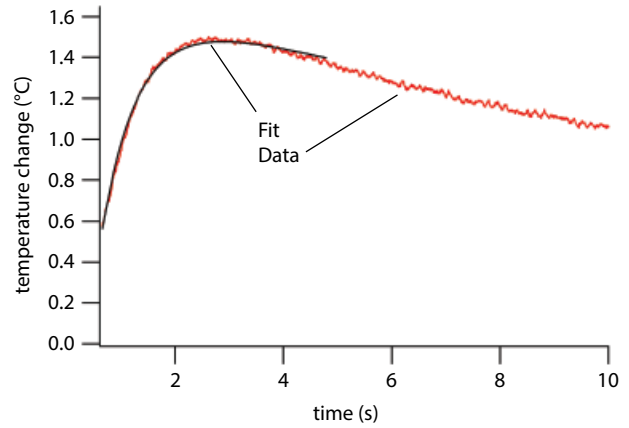


Figure 6.14 Temperature record (red) for a thermocouple 2.6 mm from a 300 MPa stick-slip event and sampled at 100 Hz. 1D model fit (black) predicts a peak temperature rise on the fault of 506 $^\circ\text{C}$ and total heat production of 36.2 kJ m^{-2} . See *electronic version for color representation*.

duration, the rate at which heat is produced at different times within a stick-slip, and buffering of temperature rise due to latent heat of fusion as gouge melts, will all contribute to errors in our calculation of peak temperature and total heat production. A sensitivity analysis of the model parameters indicates that a 10% error in T^* results in $\sim 3.5\%$ error in peak temperature. Assuming uniform heat production during a stick-slip gives a lower bound on peak temperature. Also, the error in peak temperature estimates varies nonlinearly with slip duration. If slip duration is only 20–40 μs as suggested by *Koizumi et al.* [2004] or *Passelègue et al.* [2013], a 1200 $^\circ\text{C}$ calculated peak temperature rise based on our event durations would instead represent $\sim 3000^\circ\text{C}$ rise and is probably unrealistic. If, on the other hand, slip duration was actually as long as 2 ms, the same 1200 $^\circ\text{C}$ estimate would be reduced to $\sim 400^\circ\text{C}$ and would be inconsistent with observations of pervasive melt.

There is a direct trade-off between peak temperature and shear zone width. Consequently, we present results of peak temperature for a range in a . Since temperature is measured at a distance $\sim 350a$, and at time $\sim 20,000 T^*$, total heat production estimates are insensitive to errors in either a or T^* . Grain crushing (creating new surface area) and melting (through latent heat of fusion) will both consume energy that would otherwise go into increasing fault temperature. While these processes can be important in the overall energy budget, they should not have a large effect on our computed peak temperature estimates. The measured thermocouple reading only responds to the actual PSS temperature. If this temperature is limited by pervasive melting, then the calculated peak temperature will reflect this reduced temperature rise. This does mean that our estimate of total heat production will not include

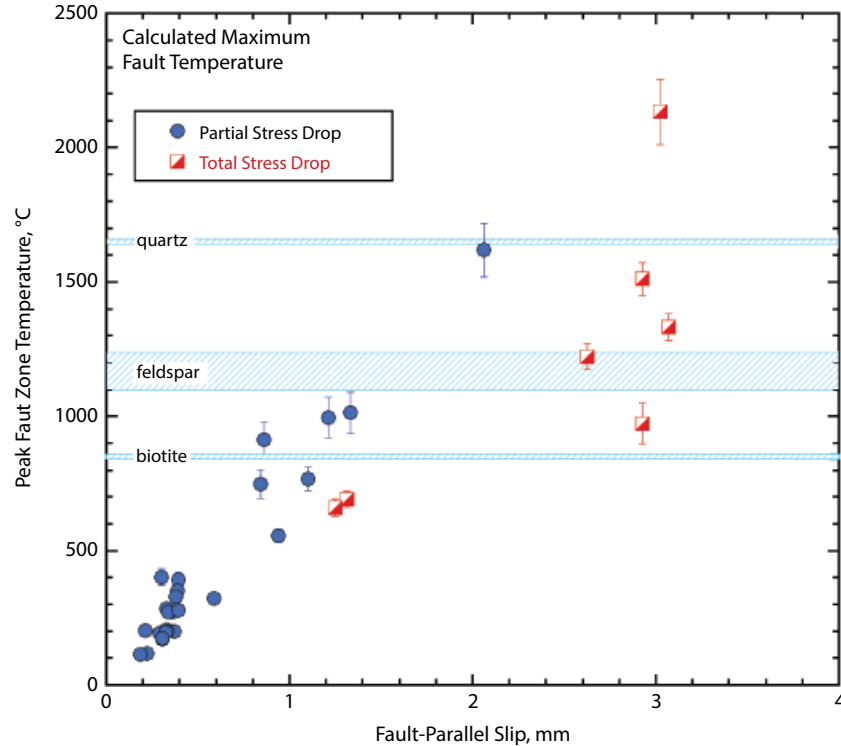


Figure 6.15 Maximum calculated surface temperature at center of PSS is plotted versus slip. Temperatures are based on matching thermocouple transients and slip duration to a 1D heat conduction model. Upper limits of error bars assume the maximum theoretical heating for zero fault thickness. Lower limits assume an average PSS thickness of $14\ \mu\text{m}$ (twice the average observed PSS thickness). Total stress drop events generally have predicted maximum temperature above the melting temperature for feldspar. In some cases, maximum temperature may exceed quartz melting temperature. See *electronic version for color representation*.

heat of fusion due to melting or heat of vitrification that is released as the melt solidifies to form a glassy surface layer. These energy terms can be estimated by knowing the width of the melt layer, heat of fusion ($\sim 64\ \text{kJ/mol}$), and heat of vitrification ($\sim 52\ \text{kJ/mol}$) [Temmer *et al.*, 2007]. We estimate uncertainty in peak temperature for the larger events of about $\pm 100^\circ\text{C}$. At intermediate confining pressures, where partial melt is developed, surface heating may be heterogeneous [Brown and Fialko, 2012], so local peak temperature may be higher than the average surface temperature computed here. Flash heating is also likely to lead to localized melting at asperity contacts well before pervasive surface melt formation occurs [Rice, 2006; Beeler *et al.*, 2008]. Accuracy in estimating total heat production will depend on thermocouple location and heterogeneity of surface heating but not on details of fault thickness or slip duration. We estimate an accuracy in total heat production of approximately $\pm 10\%$.

Results of the temperature calculations are plotted as a function of total slip in Figure 6.15. The lower bound of error bars is determined by assuming uniform deformation of a $14\ \mu\text{m}$ wide slip surface. Thermal weakening and other processes may reduce the PSS to submicron thick-

ness. Therefore, as an upper bound for the error bars, we use the limiting temperature for a shear zone with zero thickness (equation [6.10]). Maximum calculated gouge temperature increases with slip and confining pressure. The largest calculated PSS temperature is in excess of 2000°C and is obtained for a total stress drop event at $400\ \text{MPa}$ confining pressure. The largest partial stress drop temperature is for a $300\ \text{MPa}$ stick-slip event with $2.06\ \text{mm}$ slip and 81% stress drop.

The same model fitting procedure that provides maximum PSS temperature also provides an estimate of total heat production on the fault surface. Total heat production is compared to total work in Figure 6.8. Both quantities increase with increasing confining pressure, but the fraction of energy release that is converted to fault heating is less for the most energetic events. As already mentioned, the heat production plotted in Figure 6.8 does not include heat required to melt the fault gouge. Melting the nonquartz fraction of a $7\ \mu\text{m}$ gouge layer requires roughly $3\ \text{kJ m}^{-2}$ or only a few percent of the typical heat production listed in Table 6.1. This is equivalent to the heat needed for about a 50°C peak temperature rise of the same fault zone.

6.4. DISCUSSION

There have been a number of studies of the mechanics of laboratory stick-slip as well as measurements of associated frictional heating. *Johnson and Scholz* [1976] demonstrated that the lumped-mass spring-slider model provided a good representation of stick-slip events in a biaxial press with $\sigma_n = 10\text{--}20$ MPa and $T^* \sim 1$ ms. *Kilgore et al.* [2017] have expanded on that study by varying machine stiffness. They show that the spring-slider model also provides a good fit to stick-slip events on a double-direct-shear apparatus at $\sigma_n = 2$ MPa and T^* of 0.3 to 1.1 ms. *Okubo and Dieterich* [1984] reported slip durations of a few ms for stick-slip on a large 2 meter fault using a direct measurement of fault velocity. *Shimamoto et al.* [1980], using a triaxial apparatus, reported slip duration of ~ 3 ms in tests on sandstone at 30 to 100 MPa confining pressure. In their experiments, stick-slip required movement of a relatively massive pressure vessel that may explain the longer event durations. Their preferred model was a two degree of freedom spring-slider. Much shorter slip durations of 0.01–0.03 ms have been suggested in recent triaxial experiments [*Passelègue et al.*, 2013; *Koizumi et al.*, 2004]. In contrast to the *Kilgore et al.* [2017] and other studies cited above, the *Passelègue et al.* [2013] and *Koizumi et al.*, [2004] studies did not measure the time dependence of fault slip directly. Rather, the short event durations were based on indirect observations and were associated with propagation of the rupture front through the sample. These times will be significantly shorter than the slip duration and have been identified in biaxial experiments [*Johnson and Scholz*, 1976; *McLaskey and Kilgore*, 2013; *McLaskey et al.*, 2014, *Passelègue et al.*, 2013].

Unlike *Shimamoto's* [1980] design, in our experimental geometry, the upper sample half is mounted adjacent to the massive pressure vessel. Consequently, most axial and lateral motion involves movement of the lower sample half and piston. Analysis of our test geometry (section 6.3.2) has shown that the sample and piston are the most compliant elements in our loading system. The stress drop from a stick-slip event will propagate down the piston, reaching the load cell and ram after approximately 0.05 ms. At this point, the hydraulic ram will begin to move. Given the large mass of the ram, after 0.3 ms (the largest estimated event duration), even for the largest stick-slip events with total slip of ~ 3 mm, the ram will have advanced less than 0.06 mm. Thus, the stick-slip events in this loading configuration are driven by elastic unloading of the sample and piston.

When the stress drop traveling down the 0.23 m-long piston encounters the more massive load cell and ram, the contrast in acoustic impedance will cause a reflected wave to travel back up the piston and arrive at the fault

approximately 0.1 ms after the start of the stick-slip. This agrees with the average slip duration of the smaller stick-slip events (Figure 6.9). This reflected pulse may control the event duration for the partial stress drop events. Measurements of stress and fluid pressure transients during stick-slip on a nearly identical machine [*Weeks*, 1980, chapter 4] showed similar results. In a series of 10 events on wet granite at 98 MPa effective confining pressure, Weeks found a bimodal distribution of shear stress drops clustering at approximately 38 and 63 MPa. Using a piezoelectric transducer between the piston and sample, he noted a single pronounced rapid stress drop for the smaller stick-slip events. However, the larger events all produced two distinct stress pulses separated by 0.1 ms. His interpretation was that the larger stick-slips were actually double events. Given the time delay between pulses, it is possible that a reflected pulse, traveling up the piston, may trigger additional slip and extend the total event duration in our experiments. The spring-slider model can also be applied as an approximation to the dynamics in these events. In this case, we use the mass of the piston and lower sample half and the dynamic unloading stiffness ($\kappa_T = 156 \times 10^6 \text{ N m}^{-1}$). Event duration for undamped motion is [*Johnson and Scholz*, 1976; *Rice and Tse*, 1986; *Kilgore et al.*, 2017]

$$T^* = \pi \sqrt{\frac{m}{\kappa_T}} \quad (6.12)$$

and results in $T^* = 0.25$ ms. This model assumes constant dynamic friction and a lumped mass driven by a separate spring. In the present case, however, the piston and sample are the spring, so a better model would have mass distributed uniformly along the spring. A dynamic model that takes into account the true geometry of the sample and loading frame may be needed for accurate characterization of the rupture dynamics. This exercise is left for future study.

Comparison of the thermocouple measurements to the 1D conductive heat flow model shows that both maximum PSS temperature and total heat production during stick-slip increase with increasing confining pressure. Estimated maximum temperatures, based on the 1D thermal model, are plotted in Figure 6.15. The maximum calculated PSS temperature is in excess of 2000°C and is obtained for a total stress drop event at 400 MPa confining pressure. Events with slip in excess of 2 mm have calculated peak temperatures over 1100°C (onset of feldspar melt) and also show pervasive surface melt features in SEM. As the PSS temperature increases, mineralogical phase changes will have a profound effect on shear strength. Granite strength quickly degrades above about 650°C [*Wong*, 1982]. First, phyllosilicate minerals

(biotite, muscovite, chlorite) will break down and release water (~850°C). In the SEM images, vesicles appear in the glassy substrate of the slip surface (Figure 6.13) and are associated with crystals of phyllosilicate minerals adjacent to the fault. This degassing within the low-permeability granite can lead to localized pore pressure buildup that would reduce the effective normal stress and therefore fault strength. The delicate glassy filaments shown in Figure 6.13c and d can only survive if they are in open chambers on the fault surface (seen in cross-section in Figure 6.13b). These are always associated with phyllosilicate grains and may be the result of opening of the fault by localized water vapor release that exceeds the normal stress (localized thermal pressurization). Similar effects have been discussed for decarbonation reactions in high-speed carbonate experiments [Han et al., 2007; Brantut et al., 2010]. Melting temperatures for feldspars are between 1100 and 1250°C and will be reduced for the fine (submicron) particles within the gouge layer. Chemical analysis of the quenched melt using the energy dispersive system indicates that they have composition of feldspars \pm biotite and may also include quartz. There is some indication in the 400 MPa experiments that quartz grains are becoming rounded or showing other signs of melting ($T_{melt} \sim 1650^\circ\text{C}$). Further study will be required to fully determine what is happening to quartz in these experiments. Since feldspar is the main constituent of the granite gouge, once its melting temperature is exceeded, a continuous layer of melt can form on the slip surface and drastically reduce shear resistance. Continuous glassy layers are observed in the 200 MPa runs (mixed with unmelted gouge particles) and have computed surface temperatures consistent with melting of feldspar. Once a continuous melt layer forms on the slip surface and reduces shear strength, additional heat production ($=\tau\delta$) will be reduced. Enthalpy of fusion of the feldspar (~64 kJ/mol, [Tenner et al., 2007]) will provide an additional energy sink. However, for a 7 μm thick gouge layer, this becomes approximately 3 kJm⁻² and is less than 1% of the heat production during stick-slip.

Two additional features of the SEM images are noteworthy. First, there is no indication that melting is sufficiently aggressive to erode the walls of the sawcut. Second, we see no indication of injection of melt into fractures in the walls of the sawcut. Apparently, there is sufficient melt produced to coat the slip surface, but not enough excess melt to become mobile and migrate out of the gouge layer. We estimate that at the end of stick-slip, the thermal half width is 5 to 10 times greater than the gouge layer, yet even in the most energetic events, there is no evidence of melt outside the gouge. Kinetics may inhibit off-fault melt formation in the short time interval that the wall rock is above the melt temperature. Alternatively, reduction in viscosity as the melted PSS continues to heat may significantly reduce shear resistance and therefore

heat production as stick-slip continues. More sophisticated calculations than the constant heat production model used here may resolve this issue.

Constant speed rotary tests at lower normal stress show fault weakening [Chang et al., 2012; Di Toro et al., 2011; Han et al., 2011] that requires displacements of 5 mm or often much more. Some weakening processes may be related to development of ultrafine gouge particles [Han et al., 2011; Reches and Lockner, 2010] or dewatering of ultrafine particle surfaces [Sammis et al., 2011]. These processes appear to require finite slip to occur and are unlikely to be controlling the onset of abrupt weakening that produces stick-slip in our experiments. However, once stick-slip has begun, they may contribute to continued weakening. High-speed measurements have been reported for local stress changes during passage of dynamic rupture events on a 2 m fault earthquake simulator [Lockner and Okubo, 1983; McLaskey and Kilgore, 2013; Okubo and Dieterich, 1984]. These experiments show a nearly constant dynamic frictional strength following the passage of the rupture front for stick-slip events involving about 100 μm total slip at normal stresses of 1–5 MPa. The relatively low normal stress and total slip in those experiments resulted in fault surface heating of only a few degrees [Lockner and Okubo, 1983]. However, in our measurements, the systematic increase in stress drop with increasing normal stress would imply a steady decrease in dynamic friction. This drop in friction may be caused by the steady increase in surface temperature for higher normal stress and larger slip events. Reduction in static strength is much more modest than this, at least up to 600°C. Wong [1982] reported strength loss of about 30% in intact granite between room temperature and 600°C. Blanpied et al. [1995] reported increasing frictional strength in dry granite gouge to over 800°C and in wet gouge at 1 $\mu\text{m s}^{-1}$ slip rate to 400°C, at which point strength rapidly dropped with further temperature increase. While flash weakening at asperity contacts may be responsible for the progressive reduction of dynamic friction at higher normal stress [Beeler et al., 2008; Rice, 2006], in principle, it should not be normal-stress dependent. Furthermore, it is difficult to demonstrate through direct observation, either during or after stick-slip, that asperity contacts have melted, although there is recent evidence for this [Passelègue, 2014]. In our experiments, the transition to continuous melt on the fault occurs at about 200 MPa confining pressure. For these conditions, we see a continuous coating of melt mixed with unmelted granular particles. The relative proportion of melt to stronger granular particles will change systematically with increasing temperature and may be responsible for the steady decrease in dynamic strength with increasing confining pressure. By 400 MPa confining pressure, discrete gouge particles are often completely converted to

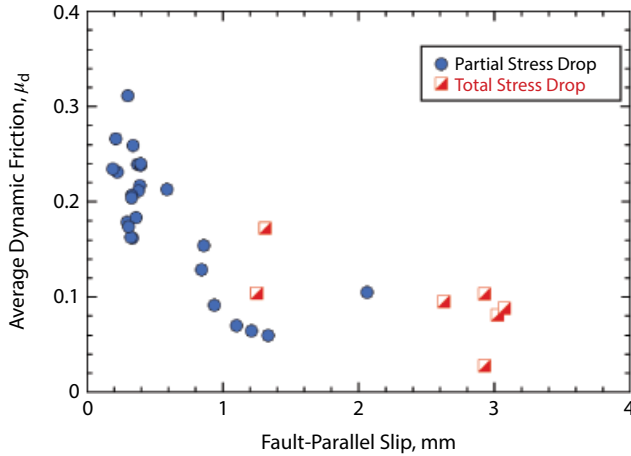


Figure 6.16 Average dynamic friction is calculated from equations (6.9) and (6.13) using thermocouple data and the observed total fault slip. Dynamic friction of high stress events is only about one third of dynamic friction of low stress events and is probably the result of thermal weakening of the PSS. See *electronic version for color representation*.

melt along the PSS. Total stress drop events that represent the maximum dynamic weakening generally show the maximum computed surface temperatures.

Because energy expended to heat the fault surface is $\int \tau_f d\delta$, average dynamic friction can be approximated by

$$\hat{\mu}_d \cong \frac{Q}{\hat{\sigma}_n \delta}. \quad (6.13)$$

This neglects work expended in fracture energy and in melt production. However, as already discussed, these terms are probably small compared to the work used to heat the fault. We plot this estimate of average dynamic friction, which is based on the thermocouple data, in Figure 6.16. Average dynamic friction for events that slid <0.5 mm is 0.22. For events that slid >2 mm, average dynamic friction drops to 0.08. This decrease in friction implies a significant weakening due to heating of the PSS. Melt formation is a likely cause of this dynamic strength loss.

We use the 1D thermal model to estimate total heat production. For a thermocouple 2–3 mm from the fault, peak temperature occurs about 2 s after the stick-slip event so that details of the precise slip duration and PSS thickness become unimportant. Calculated heat production is plotted in Figure 6.8 as green and purple squares, representing partial and total stress drop events, respectively. In addition, total energy release is plotted in blue (normal stick-slip) and red (total stress drop events). Total energy is calculated from static axial force (before and after each stick-slip) and fault slip. Therefore, the estimates of total energy and heat production are obtained by completely independent measurements. Heat production accounts for about 50% of the energy release for the small stick-slip

events and drops to less than 20% of energy release for the total stress drop events. This is consistent with a systematic decrease in dynamic friction at high confining pressure due to surface melt and reduced shear resistance. As a result, the relative efficiency of generating surface heat is reduced and a greater proportion of energy release is radiated away from the fault. Work expended in crushing fault gouge particles and in melting the PSS is not included in the plotted heat production. Energy consumed in grain comminution is unknown but generally considered to be small in this bare surface fault geometry. Much of the initial grain comminution in the 7 μ m gouge layer occurs quasi-statically during creep on the sawcut before the first stick-slip event. Examples of this creep are shown in Figure 6.2 during strain hardening prior to the first stick-slip. Given the observed fault width, feldspar melt formation is roughly 3 kJ m^{-2} and within the measurement uncertainty plotted in Figure 6.8. An additional unknown factor is the influence of increasing viscosity of the silicone oil confining fluid with increasing confining pressure. Since the lower sample half shifts laterally during stick-slip, it forces movement of the oil in the pressure chamber. Viscous drag will increase at higher confining pressure and will consume additional energy. In future experiments we will assess the importance of viscous drag in the energy balance by replacing silicone oil with argon gas. For now, we do not know the importance of this effect in influencing stick-slip characteristics.

The thermal half width of a dynamic event will increase roughly as $\sqrt{T^*}$. This means that longer event duration can heat a wider zone and therefore limit the peak temperature, even if the PSS is narrow. For stick-slip events reported here, slip duration is less than 1 ms and $\alpha_0 = 20$ to 50 μ m. For an earthquake with slip duration of 1 to 10 s, the thermal half width can increase to 2–7 mm, and reduce the peak temperature to 1% of the peak temperature produced in our experiments. Thus, shear stress, gouge width, slip speed, and slip duration all contribute to the maximum temperature attained during an earthquake, as discussed by *Cardwell et al.* [1978] and *Lachenbruch* [1980].

The general stick-slip behavior and how it varies with confining pressure can be illustrated with a single-degree-of-freedom spring-slider model. We carried out simulations that are intended to show general trends in behavior rather than a precise match to the observed measurements. The model we use has constant static friction ($\mu_s = 0.7$) and temperature-dependent dynamic friction, with μ_d decreasing linearly between 700°C and 1200°C to approximate the effects of increasing partial melt:

$$\begin{aligned} \mu_d &= 0.60 & \theta < 700^\circ\text{C} \\ \mu_d &= 1.37 - 0.0011\theta & 700^\circ\text{C} \leq \theta \leq 1200^\circ\text{C} \\ & & \text{(linear decrease in } \mu_d \text{)} \\ \mu_d &= 0.05 & \theta > 1200^\circ\text{C}. \end{aligned} \quad (6.14)$$

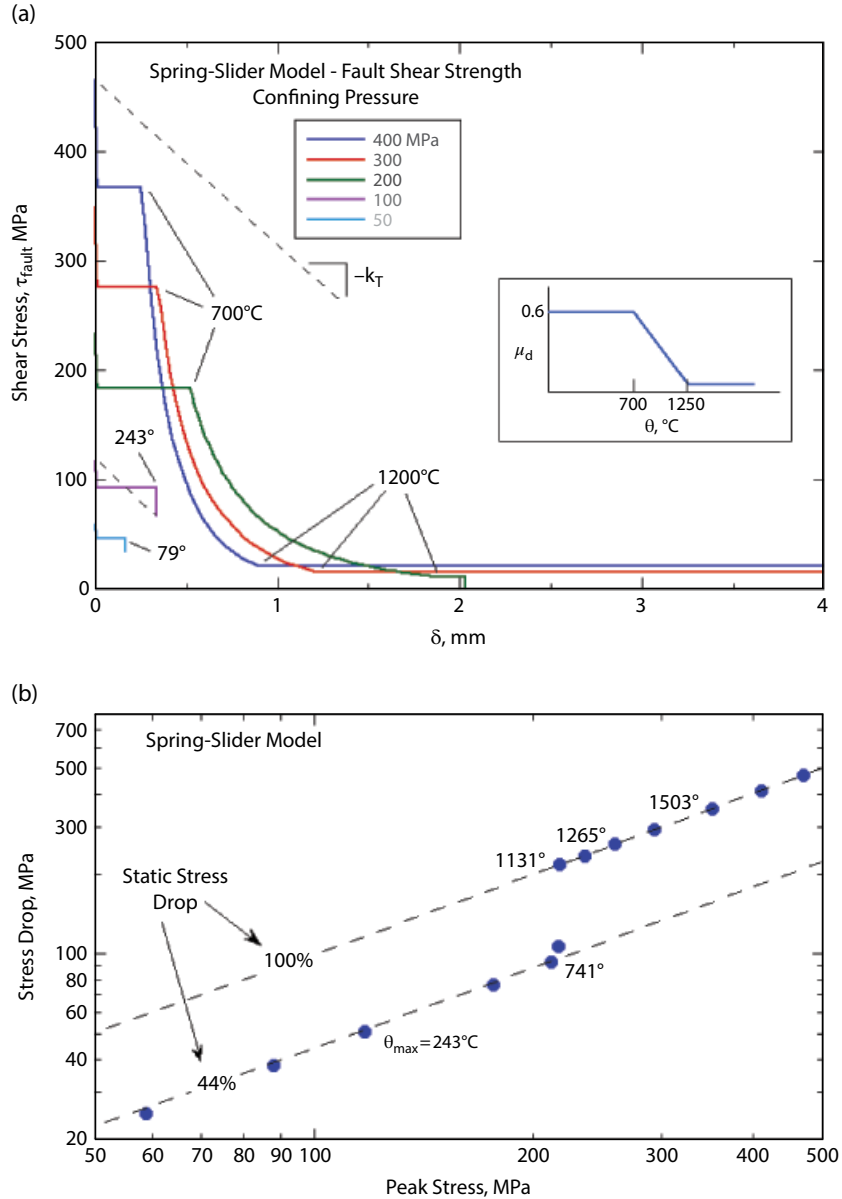


Figure 6.17 (a) Spring-slider model for stick-slip events using temperature-dependent dynamic friction (see insert). At low confining pressure (50 and 100 MPa) the fault does not reach thermal weakening temperature. As confining pressure increases, the onset of thermal weakening occurs at progressively shorter displacement. (b) Stress drop plotted versus peak stress. Maximum fault temperature is shown for selected runs. At low confining pressure, the constant ratio of μ_d/μ_s results in a constant 44% stress drop for the simple spring-slider model. However, the onset of thermal weakening produces a large, delayed stress drop that results in total stress drop stick-slip events. The transition to total stress drop events in the experimental data (Figure 6.5) is more gradual and may represent a more complex temperature and velocity-dependent fault rheology or may indicate that a distributed mass dynamic model is needed to describe the system response. See *electronic version for color representation*.

This simple model has no radiated energy loss so that some small high-temperature dynamic friction must be included to bring the fault to rest. As with actual experiments, simulations are run at constant confining pressure that, in combination with the prescribed friction, determines τ_f and σ_n according to equation (6.3). An unloading

machine stiffness of $k_T = 150 \text{ MPa/mm}$ is assumed and a single value of mass m is chosen to give slip duration in all simulations of 0.1–0.3 ms. The initial conditions in each simulation have the fault at rest and τ_f and σ_n prescribed by μ_s and P_c . Then, fault strength is spontaneously dropped to μ_d . In each time step, acceleration,

velocity, and displacement are calculated and an increment of frictional heating is added to the fault temperature according to $\Delta\theta = 0.54\theta_{\max}$, where θ_{\max} is the thin fault limiting temperature (equation [6.10]). The factor of 0.54 is consistent with the reduced temperature rise for a finite-width fault that is smaller than the thermal width [Cardwell *et al.*, 1978]. While this is only an approximate representation of the 1D diffusion equation, it is sufficient for our purposes. The new fault temperature is used to adjust μ_d for the next time step.

Simulations between 50 and 400 MPa confining pressure are shown in Figure 6.17a. In all cases, the initial sliding resistance is constant ($\mu_d = 0.6$) as the fault heats. At 100 MPa, the fault temperature is 243°C by the end of the stick-slip, and after sliding at constant shear stress τ_f drops to match the applied machine load represented by the dashed line. At $P_c = 200$ MPa, fault temperature has risen to 700°C at 0.53 mm and fault weakening continues until the surface temperature reaches 1200°C at 1.89 mm slip. This is a total stress drop event and shear stress drops to zero when sliding stops at 2.03 mm. Due to the higher stress in the 300 and 400 MPa simulations, weakening begins at progressively shorter slip. Both of these are also total stress drop events. Static stress drops for a suite of runs that include these simulations, plotted in Figure 6.17b. For the simplified friction model used in these calculations, the lower temperature runs have a constant stress drop of 44%. Then, with the onset of surface melting, static stress drop abruptly jumps to 100%. Some additional complexity in fault rheology is needed to reproduce the more gradual increase in stress drop that is observed in the experimental data (Figure 6.5).

A characteristic feature of the spring-slider model is that for constant dynamic friction, the event duration is independent of stress drop and is controlled by mass and stiffness (equation [6.12]). However, in the simulations plotted in Figure 6.17, there is a double stress drop. First, shear resistance is reduced to the low temperature value of $\mu_d = 0.6$ and then, fault heating provides a second later stress drop. The delay in the onset of the second stress drop results in extending the total time of the stick-slip event beyond the duration predicted by equation (6.12). This effect may contribute to the systematic lengthening of T^* for the larger stick-slip events shown in Figure 6.9. In addition, the fixed slip duration in the spring-slider model will only be valid for partial stress drops in which the driving force decreases linearly with displacement. For a total stress drop event, this is no longer the case and once the driving stress drops to zero, the moving block can continue to slide much farther with no additional restoring force trying to bring it to rest. This is likely to be an additional contributing factor in the large displacements observed in some of the total stress drop events.

The pseudotachylite formation reported here would represent an unusual case for naturally occurring earthquakes. Rupture is short, intense, and on a thin, smooth, dry fault surface. The total stress drop associated with surface melting in our experiments is not common for earthquakes, although a small number of large stress drop earthquakes have been reported. Kilgore *et al.* [2017] point out that the limited sample size in most laboratory experiments leads to breakout of the rupture to a free surface so that loading frame stiffness controls rupture duration rather than back-propagation of stopping phases for natural earthquakes. There are exceptions to this situation in the laboratory. Lockner *et al.* [1982] were able to arrest stick-slip in a large biaxial press by destressing the ends of the fault before rupture. Also, acoustic emissions are naturally occurring dynamic instabilities that can be contained on fault surfaces and that, although they are small, are indistinguishable in other aspects from natural earthquakes [McLaskey and Kilgore, 2013; McLaskey and Lockner, 2014]. Still, total stress drops during stick-slip may be related to the limited sample size and boundary conditions in laboratory tests as compared to earthquakes.

While normal stresses in these experiments are consistent with earthquakes that occur at mid crustal or subduction zone conditions, slip during large earthquakes is substantially greater than the 1 to 3 mm obtained here. Larger slip implies that wider PSS could be heated to melting conditions than the 10-micron-scale slip surfaces generated here. Since crustal and megathrust faults are generally wet, the heating and vaporizing of fluids, with the possibility of reduced effective normal stress, could limit frictional heating and prevent melt formation. This may be a common occurrence in natural earthquakes. Now that we have placed constraints on heating of dry laboratory fault surfaces at elevated normal stress, future work will involve stick-slip on wet faults and the conditions needed to develop fluid pressurization [e.g., Proctor and Lockner, 2016]. Even though dynamic laboratory events are rapid, the convenience of producing high stress and controlled pore pressure, both at room and elevated temperature, make triaxial stick-slip experiments appealing for investigating dynamic rupture processes.

6.5. CONCLUSIONS

A total of 112 stick-slip events were generated on bare surface granite sawcut samples spanning a decade range of confining pressure and normal stress. Strength, stress drop, slip, duration, average slip speed, surface temperature, and heat production all increased with increasing confining pressure. Average dynamic friction systematically decreased with confining pressure and resulted in total stress drops for most events above $P_c = 200$ MPa.

SEM observations showed that extensive surface melt formed in experiments above about $P_c = 200$ MPa. At the highest confining pressure, slip surfaces contained open chambers with delicate glassy filaments and degassing vents adjacent to phyllosilicate minerals. Some of the open voids were a few microns in height and had lateral extent in excess of $50\ \mu\text{m}$. Average gouge layer thickness was $7\ \mu\text{m}$, but the active slip surface during stick-slip may have been much narrower than that. Event duration was estimated to range from about 0.1 to 0.3 ms, resulting in a thermal half width at the end of stick-slip of 22 to $38\ \mu\text{m}$. Details of the timing of strength loss due to melt formation and temperature-dependent viscosity will have important implications for the timing of heat production and the efficiency of seismic radiation. These considerations are beyond the scope of the present study but will be important in applying laboratory results to natural earthquakes. While a lumped-mass spring-slider model may provide an adequate representation of the stick-slip dynamics, the physical dimensions of the sample and loading frame suggest that a more elaborate distributed mass model may be necessary to understand the detailed slip response. When more precise near-field measurements of stress and displacement are obtained, this issue will be addressed in greater detail. The experiments reported here provide a unique way of measuring coseismic fault properties at in situ stresses. One advantage of the triaxial apparatus is that elevated ambient temperature and pore pressure can be added in a relatively routine manner to allow for more accurate replication of natural conditions that exist at depth on seismogenic faults.

ACKNOWLEDGMENTS

We thank S. Cox, A. McGarr, G. McLaskey, and A. Schubnel for thoughtful comments that greatly improved the manuscript. Any use of trade, firm, or product names is for descriptive purposes only and does not imply endorsement by the U.S. Government. We also acknowledge J. Weeks for his innovative high-speed measurements of stick-slip processes that remained unsurpassed for over 30 years.

REFERENCES

- Andrews, D. J. (2002), A fault constitutive relation accounting for thermal pressurization of pore fluid, *J. Geophys. Res.*, *107*, doi:10.1029/2002JB001942.
- Beeler, N. M., T. E. Tullis, and D. L. Goldsby (2008), Constitutive relationships and physical basis of fault strength due to flash heating, *J. Geophys. Res.*, *113*(B01401), doi:10.1029/2007JB004988.
- Beeler, N. M., T. Tullis, J. Junger, B. Kilgore, and D. Goldsby (2014), Laboratory constraints on models of earthquake recurrence, *J. Geophys. Res.*, *119*, 8770–8791, doi:10.1002/2014JB011184.
- Blanpied, M. L., D. A. Lockner, and J. D. Byerlee (1995), Frictional slip of granite at hydrothermal conditions, *J. Geophys. Res.*, *100*(B7), 13,045–13,064.
- Brace, W. F., and J. D. Byerlee (1966), Stick slip as a mechanism for earthquakes, *Science*, *153*, 990–992.
- Brantut, N., F. X. Passelègue, D. Deldicque, J. Rouzaud, and A. Schubnel (2016), Dynamic weakening and amorphization in serpentinite during laboratory earthquakes, *Geology*, *44*(8), 607–610, doi:10.1130/G37932.1.
- Brantut, N., A. Schubnel, J. Corvisier, and J. Sarout (2010), Thermochemical pressurization of faults during coseismic slip, *J. Geophys. Res.*, *115*(B5).
- Brantut, N., A. Schubnel, J. Rouzaud, F. Brunet, and T. Shimamoto (2008), High-velocity frictional properties of a clay-bearing fault gouge and implications for earthquake mechanics, *J. Geophys. Res.*, *113*(B10).
- Brown, K., and Y. Fialko (2012), ‘Melt welt’ mechanism of extreme weakening of gabbro at seismic slip rates, *Nature*, *488*, 638–641, doi:10.1038/nature11370.
- Byerlee, J. D. (1978), Friction of rocks, *Pure Appl. Geophys.*, *116*, 615–626.
- Cardwell, R. K., D. S. Chinn, G. F. Moore, and D. L. Turcotte (1978), Frictional heating on a fault zone with finite thickness, *Geophys. J. R. Astr. Soc.*, *52*, 525–530.
- Chang, J. C., D. A. Lockner, and Z. Reches (2012), Rapid acceleration leads to rapid weakening in earthquake-like laboratory experiments, *Science*, *338*, 101–105, doi:10.1126/science.1221195.
- Di Toro, G., D. Goldsby, and T. E. Tullis (2004), Friction falls towards zero in quartz rock as slip velocity approaches seismic rates, *Nature*, *427*, 436–439.
- Di Toro, G., R. Han, T. Hirose, N. De Pao, S. Nielsen, K. Mizoguchi, F. Ferri, M. Cocco, and T. Shimamoto (2011), Fault lubrication during earthquakes, *Nature*, *471*, 494–499, doi:10.1038/nature09838.
- Di Toro, G., T. Hirose, S. Nielsen, G. Pennacchioni, and T. Shimamoto (2006), Natural and experimental evidence of melt lubrication of faults during earthquakes, *Science*, *311*.
- Di Toro, G., G. Pennacchioni, and S. Nielsen (2009), Pseudotachylites and earthquake source mechanics, in *Fault-Zone Properties and Earthquake Rupture Dynamics*, edited by E. Fukuyama, pp. 87–133.
- Han, R., T. Hirose, T. Shimamoto, Y. Lee, and J. Ando (2011), Granular nanoparticles lubricate faults during seismic slip, *Geology*, *39*(6), 599–602, doi:10.1130/G31842.1.
- Han, R., T. Shimamoto, T. Hirose, J.-H. Ree, and J. Ando (2007), Ultralow friction of carbonate faults caused by thermal decomposition, *Science*, *316*, 878–881, doi:10.1126/science.1139763.
- Hirose, T., and T. Shimamoto (2005), Growth of molten zone as a mechanism of slip weakening of simulated faults in gabbro during frictional melting, *J. Geophys. Res.*, *110*.
- Jiang, H., C.-T. Lee, J. Morgan, and C. Ross (2015), Geochemistry and thermodynamics of an earthquake: A case study of pseudotachylites within mylonitic granitoid, *Earth and Planetary Sci. Lett.*, *430*, 235–248, doi:http://dx.doi.org/10.1016/j.epsl.2015.08.027.
- Johnson, T. L., and C. H. Scholz (1976), Dynamic properties of stick-slip friction of rock, *J. Geophys. Res.*, *81*, 881–888.

- Karner, S. L., and C. Marone (2000), Effects of loading rate and normal stress on stress drop and stick-slip recurrence interval, in *Geocomplexity and the Physics of Earthquakes*, Geophys. Monogr. Ser., vol. 120, edited by J. B. Rundle *et al.*, pp. 187–198, AGU, Washington, D. C.
- Kilgore, B. D., A. McGarr, N. M. Beeler, and D. A. Lockner (2017), Earthquake source properties from instrumented laboratory stick-slip, in *AGU Monographs, Fault Zone Dynamic Processes: Evolution of Fault Properties During Seismic Rupture*, edited by M. Y. Thomas, T. Mitchell, and H. S. Bhat (this volume).
- Koizumi, Y., K. Otsuki, A. Takeuchi, and H. Nagahama (2004), Frictional melting can terminate seismic slips: Experimental results of stick-slips, *Geophys. Res. Lett.*, *31*(L21605), doi:10.1029/2004GL020642.
- Lachenbruch, A. H. (1980), Frictional heating, fluid pressure, and the resistance to fault motion, *J. Geophys. Res.*, *85*(B11), 6097–6112.
- Lockner, D. A., and P. G. Okubo (1983), Measurements of frictional heating in granite, *J. Geophys. Res.*, *88*, 4313–4320.
- Lockner, D. A., P. G. Okubo, and J. H. Dieterich (1982), Containment of stick-slip failures on a simulated fault by pore fluid injection, *Geophys. Res. Lett.*, *9*, 801–804.
- McGarr, A., and J. Fletcher (2007), Near-fault peak ground velocity from earthquake and laboratory data, *Bul. Seism. Soc. Amer.*, *97*(5), 1502–1510, doi:10.1785/0120060268.
- McLaskey, G. C., and B. Kilgore (2013), Foreshocks during the nucleation of stick-slip instability, *J. Geophys. Res.*, *118*, 1–16, doi:10.1002/jgrb.50232.
- McLaskey, G. C., B. D. Kilgore, D. A. Lockner, and N. M. Beeler (2014), Laboratory generated M -6 earthquakes, *Pure App. Geophys.*, *171*(10), 2601–2615, doi:10.1007/s00024-013-0772-9.
- McLaskey, G. C., and D. A. Lockner (2014), Preslip and cascade processes initiate laboratory stick-slip, *J. Geophys. Res.*, *119*(8), 6323–6336, doi:10.1002/2014JB011220.
- Moore, D. E., D. A. Lockner, N. M. Beeler, and B. D. Kilgore (2016), Gallery of melt textures developed in Westerly Granite during high-pressure triaxial friction experiments, *U.S. Geological Survey Open File Report, 2016-1059*, 75 p., doi:http://dx.doi.org/10.3133/ofr20161059.
- Nielsen, S., G. Di Toro, T. Hirose, and T. Shimamoto (2008), Frictional melt and seismic slip, *J. Geophys. Res.*, *113*.
- Noda, H., E. Dunham, and J. R. Rice (2009), Earthquake ruptures with thermal weakening and the operation of major faults at low overall stress levels, *J. Geophys. Res.*, *114*, doi:10.1029/2008JB006143, 2009.
- Okubo, P. G., and J. H. Dieterich (1984), Effects of physical fault properties on frictional instabilities produced on simulated faults, *J. Geophys. Res.*, *89*, 5815–5827, doi:10.1029/JB089iB07p05817.
- Passelègue, F. X. (2014), *Experimental study of the seismic rupture*, PhD thesis, Ecole Normale Supérieure de Paris, available at ftp://ftp.geologie.ens.fr/incoming/tempo/passelegue/PhDFXP.pdf, 193 p.
- Passelègue, F. X., A. Schubnel, S. Nielsen, H. S. Bhat, and R. Madariag (2013), From sub-Rayleigh to supershear ruptures during stick-slip experiments on crustal rocks, *Science*, *340*, 1208–1211, doi:10.1126/science.1235637.
- Proctor, B., and D. A. Lockner (2016), Pseudotachylyte increases the post-slip strength of faults, *Geology*, *44*, 1003–1006.
- Reches, Z., and D. A. Lockner (2010), Fault weakening and earthquake instability by powder lubrication, *Nature*, *467*, 452–455, doi:10.1038/nature09348.
- Rice, J. R. (2006), Heating and weakening of faults during earthquake slip, *J. Geophys. Res.*, *111*, doi:10.1029/2005JB004006.
- Rice, J. R., and S. T. Tse (1986), Dynamic motion of a single degree of freedom system following a rate and state dependent friction law, *J. Geophys. Res.*, *91*, 521–530.
- Sammis, C., D. A. Lockner, and Z. Reches (2011), The role of adsorbed water on the friction of a layer of submicron particles, *Pure App. Geophys.*, *168*(12), 2325–2334, doi:10.1007/s00024-011-0324-0.
- Shimamoto, T., J. Handin, and J. Logan (1980), Specimen-apparatus interaction during stick-slip in a triaxial compression machine: A decoupled two-degree-of-freedom model, *Tectonophysics*, *67*, 175–205.
- Sibson, R. (1975), Generation of pseudotachylyte by ancient seismic faulting, *Geophys. J. R. Astron. Soc.*, *43*, 775–794.
- Spray, J. G. (1987), Artificial generation of pseudotachylyte using friction welding apparatus: Simulation of melting on a fault plane, *J. Struct. Geol.*, *9*, 49–60.
- Spray, J. G. (2010), Frictional melting processes in planetary materials: From hypervelocity impact to earthquakes, *Annu. Rev. Earth Planet. Sci.*, *38*, 221–254, doi:10.1146/annurev.earth.031208.100045.
- Sulem, J., and V. Famin (2009), Thermal decomposition of carbonates in fault zones: Slip-weakening and temperature-limiting effects, *J. Geophys. Res.*, *114*(B3).
- Summers, R., and J. Byerlee (1977), Summary of results of frictional sliding studies, at confining pressures up to 6.98 kb, in selected rock materials, *U.S. Geological Survey, Open File Report 77-142*, 129 p.
- Tembe, S., D. A. Lockner, and T.-f. Wong (2010), Effect of clay content and mineralogy on frictional sliding behavior of simulated gouges: Binary and ternary mixtures of quartz, illite and montmorillonite, *J. Geophys. Res.*, *115*(B03416), doi:10.1029/2009JB006383.
- Tenner, T. J., R. A. Lange, and R. T. Downs (2007), The albite fusion curve re-examined: New experiments and the high-pressure density and compressibility of high albite and NaAlSi₃O₈ liquid, *American Mineralogist*, *92*, 1573–1585, doi:10.2138/am.2007.2464.
- Teufel, L. W., and J. M. Logan (1978), Effect of displacement rate on the real area of contact and temperatures generated during frictional sliding of Tennessee sandstone, *Pure Appl. Geophys.*, *116*, 840–872.
- Weeks, J. D. (1980), Some aspects of frictional sliding at high normal stress, PhD Thesis, Stanford University, Stanford, California, 171 p.
- Wong, T.-f. (1982), Effects of temperature and pressure on failure and post-failure behavior of Westerly granite, *Mechanics of Materials*, *1*, 3–17.